A SEMI-INVERSE DESIGN TECHNIQUE FOR LEADING EDGE SLATS

Thesis by

John Edwin O'Pray

In Partial Fulfillment of the Requirements

for the Degree of

Aeronautical Engineer

California Institute of Technology

Pasadena, California

1970

(Submitted May 29, 1970)

ACKNOWLEDGEMENT

The author wishes to express his appreciation to Dr. Peter Lissaman for his guidance and encouragement during this study. Mr. A. M. O. Smith of the Douglas Aircraft Company generously made available the Douglas-Neumann direct numerical solutions. The assistance of Mrs. Roberta Duffy and Mrs. Elizabeth Fox in the preparation and typing of the manuscript is gratefully recognized.

ABSTRACT

A design technique for analytically generating a leading edge slat which will induce the modulating field required to match a specified pressure distribution on the nose of an elliptical airfoil was developed. This planar potential flow solution can be readily generalized to the design of slats to prevent boundary-layer separation at the nose of an arbitrary airfoil. The technique is described as semi-inverse because the singularity representation for the slat is constrained so that only realistic slat shapes will be generated.

The elliptical airfoil is mapped to a half-plane. In this domain, the slat is represented by a finite series of distributed singularities on an inclined chord line which is placed along a zero order nose flow streamline. These distributed singularities correspond to the singular and regular camber and thickness modes of thin airfoil theory. A suitable slat chord location in the half-plane is selected by examination of the distribution of the specified modulating velocity. For a fixed slat location, the slat-induced velocity field can be written explicitly in terms of the unknown series coefficients. A least squares matching to the specified modulating field is used to select the coefficients. The velocity distribution along the chord line is integrated to determine the slat surface streamlines which are then transformed back to the ellipse plane.

The digital computer program for the semi-inverse solution can be executed rapidly. Once an appropriate slat chord location in

the half-plane has been selected, an accurate matching of the specified pressure distribution on the airfoil can be achieved. The airfoil nose flow calculated by the semi-inverse solution agrees very closely with the flow computed by the Douglas-Neumann direct solution for the same slat geometry.

The airfoil nose flow is very sensitive to the distribution of camber and thickness along the chord line. In some test cases, a modified semi-inverse solution was required in which the minimum acceptable slat thickness was prescribed and a restricted inversion solution was conducted to select the camber mode coefficients required to match the specified modulating field. For a thin airfoil with a severe nose suction peak, a small, thin, highly-cambered slat which is located close to the airfoil nose is desirable.

TABLE OF CONTENTS

TABLE OF CONTENTS (Cont'd)

LIST OF FIGURES

NOMENCLATURE

B_I slat singularity distribution mode coefficient

c_2 slat chord in half-plane

c_3 radius of airfoil circle

f_1 slat midchord height above real axis in half-plane

f_2 slat midchord offset from origin in half-plane

h_i half-plane coordinate x_{i3} of the i^{th} matching station

i as subscript, index corresponding to the i^{th} matching station

k_6 slat inclination with respect to real axis in half-plane

R_0 ellipse nose radius

$S = s+it$ slat plane coordinates

U onset flow velocity in ellipse plane

u_{iI} influence coefficient corresponding to the I^{th} slat singularity distribution mode

$W = x_3+iy_3$ half-plane coordinates

w_{i1} slat-induced velocity at h_i in half-plane

w_{i2} specified modulating velocity at h_i in half-plane

w'_{i2} biased specified modulating velocity at h_i in half-plane

w_{i3} main flow velocity at h_i in half-plane

w_{i4} specified velocity at h_i in half-plane

w_{i5} offset velocity at h_i in half-plane

$Z = x_1+iy_1$ ellipse plane coordinates

$z = x_2+iy_2$ circle plane coordinates

α ellipse angle of attack

Γ_0 basic ellipse circulation, no slat

NOMENCLATURE (Cont'd)

Γ_s	slat circulation
Γ_c	compensating circulation required on ellipse when slat is added
Γ_t	total ellipse circulation
ζ	slat circle plane variable
τ	maximum-thickness-to-chord ratio of ellipse
τ_s	maximum-thickness-to-chord ratio of slat in slat plane

I. INTRODUCTION

A leading edge slat is an auxiliary airfoil located ahead of the nose of the main airfoil to prevent separation of the airfoil boundary layer near the leading edge. Usually employed in conjunction with trailing edge flaps, a leading edge slat raises the maximum lift coefficient of the airfoil by delaying the onset of nose stall as the angle of attack increases. The circulation around the heavily loaded slat superimposes a backflow component on the high-speed flow around the airfoil nose, thereby lowering the peak velocity and decreasing the pressure gradient behind the minimum pressure point. Therefore, the leading edge slat is, in a sense, a boundary layer control device, because the slat alters the pressure gradient history experienced by the main airfoil boundary layer.

The concept of the "slotted wing" was initially developed by Lachmann and Handley Page and was widely used during the 1920's on outer wing sections to prevent tip stalling and incipient spin. Fixed leading edge slats are still employed in some STOL aircraft designed only for low speed operation, and a typical configuration is shown in Figure 1-A (1, Fig. 10).

Prior to World War II, extensive wind tunnel tests of various configurations of fixed "auxiliary airfoils" were conducted by the National Advisory Committee for Aeronautics. A typical configuration evaluated by Weick and Sanders (2) is shown in Figure 1-B. Thick airfoil sections which have broad nose velocity peaks and large slats with chords of 15 to 25 percent of the main airfoil chord were used. These fixed slat configurations represented a

compromise between maximum low-speed lift and minimum cruise drag. In the limited experimental parameter studies, the ratio ($C^2_{L_{max}}/C_{D_{min}}$) was optimized.

As aircraft cruise speeds increased, retractable slat designs were developed. Because thin airfoil sections develop high nose suction peaks at the lift coefficients required for takeoff and for landing approach, small, highly-cambered slats located close to the nose of the main airfoil are required to prevent separation. The NACA 64_1A212 airfoil with leading edge slat and slotted flap tested by Quinn (3) is a typical example of retractable slat design circa 1947, and is shown in Figure 1-C. Without boundary layer suction on the main airfoil, the addition of the slat increased the maximum lift coefficient by .48 to 3.30, and, with suction at 40 percent of chord, $\Delta C_{L_{max}} = .74$ was obtained. Current retractable designs, such as the slat on the DC-9 Series 30, are much smaller and closer to the airfoil nose than the earlier configurations, but the lines of such current designs are proprietary and therefore unavailable for publication. For comparison, the slat configuration β70 designed by the semi-inverse technique of this thesis is shown in Figure 13.

The NACA experiments demonstrated that the performance of a slatted airfoil was highly sensitive to slat shape and position. This sensitivity to slat geometry is due to the large local velocity gradients in the highly curved flow field around the nose of an airfoil operating at a high lift coefficient. Because of the impracticality of wind tunnel testing of a full range of slat chords and camber and

thickness distributions, experimental "optimization" of a slat design was and still is generally limited to the determination of the best location for a slat of fixed shape. In the typical test series conducted by Quinn (3), the slat trailing edge location required to maximize $C_{L_{max}}$ was determined for three slat orientations.

Before the advent of digital computers, theoretical analysis of leading edge slats was generally limited to planar-potential-flow direct solutions by conformal mappings for a few special slat and airfoil shapes having convenient transformations. In a survey article in Boundary Layer and Flow Control, Lindfield (4) describes several of these direct solutions which were published in foreign journals. In Lachmann's 1923 solution, the slat was represented by a lattice of point vortices and the main airfoil by a Joukowski section. Golubev's solution was similarly restricted to Joukowski sections, but Strassl's complete mapping solution employed the Kármán-Trefftz transformation which permits a finite trailing edge angle on the main airfoil. Golubev's direct solution incorporated a laminar boundary-layer analysis by the Pohlausen method to predict whether separation would occur under the pressure gradients imposed by the potential flow solution including a point vortex representing a slat.

Since large digital computers are now so readily available, a number of fully nonlinear, direct solution techniques such as the Douglas-Neumann method (5) have been developed. These numerical techniques provide highly accurate potential flow solutions for a fixed geometry. The direct problem, the solution for the pressure distribution on a slat and airfoil of arbitrarily specified

shape, can be regarded as solved.

However, in current design practice, the inverse problem is of equally great importance. A thin wing with a small radius nose carefully shaped to optimize the pressure distribution for high-speed cruise will rapidly develop an unacceptably high nose suction peak as the angle of attack increases. Given such an airfoil, an inverse solution for a slat shape and position which will produce an acceptable velocity distribution on the airfoil nose is then required. An approximate solution for this inverse problem is presented in this thesis.

The inverse problem can be posed in the following form. For an arbitrary airfoil at a specified lift coefficient, generate a class of leading edge slats which will induce suitable pressure modulations on the nose of the airfoil to prevent boundary layer separation. This thesis does not attempt to define an "optimum" slat since such a measure of effectiveness involves numerous practical design considerations. For example, the structural strength of the slat and potential aeroelastic effects as well as provision for slat retraction into or on top of the airfoil nose must be considered by the designer. The semi-inverse slat design technique presented in this thesis allows the designer reasonable freedom to specify the slat chord and location to satisfy such non-aerodynamic constraints and then generates a slat shape which will induce approximately the specified velocity field on the airfoil.

Designing a slat for proper nose flow modulation at a single

specified lift coefficient is quite realistic because leading edge slats are employed primarily for the closely-defined, steady-state flight during approach for landing and climbout after liftoff. If efficient slat performance under off-design conditions is a requirement, a designer can adopt a slat geometry representing a compromise between two single-design-point slats or can employ a variable camber slat.

For the inverse slat design problem, the planar potential flow assumption introduces the analytic convenience of complex variables and does not unduly restrict the physical relevance of the solution. The boundary layer on the airfoil experiences an extremely favorable pressure gradient from the stagnation point forward to the point of minimum pressure, and thus it can be expected to be thin with respect to the slat gap. Experimental studies such as Lachmann's (4, 189) support this approximation. For an inverse solution, the pressure gradient on the airfoil nose can, in principle, be explicitly specified to avoid local boundary-layer separation. The validity of the implicit assumption that the flow on the slat is attached can be checked after the inverse solution by direct boundary-layer calculations using the predicted inviscid pressure distribution on the slat. Because leading edge slats are normally deployed at low airspeeds for takeoff and landing approach, the assumption of incompressible flow is justified. Except for the case of slats on highly swept wings where the spanwise crossflow may be significant, the two-dimensionality assumed in this planar

potential flow solution is not highly restrictive.

The goal of this thesis is a semi-inverse approximate solution which is constrained to produce a physically realizable slat configuration. In principle, after mapping the airfoil to a circle, an exact distribution of singularities corresponding to an arbitrary specified velocity on the circle could be determined. For example, by assuming a power series representation for the velocity field outside the airfoil circle, the singularities could be located by numerical determination of the points at which the series diverges. However, for an arbitrary specified velocity distribution, the closure and uniqueness conditions for such an unconstrained inverse solution are unknown. Absolute closure of the singularity flow field requires that the sum of source and sink flows be zero, but this does not insure that there will be a single closed slat streamline, nor does it preclude re-entrant shapes. Furthermore, the uniqueness of an unconstrained inverse solution is dubious. For example, consider the classical ambiguity of the identical external fields induced by a point vortex or by any concentric circle with vorticity uniformly distributed on its circumference and having the same circulation as the point vortex. The general problem of an inverse solution for unknown singularities at unknown locations appears to be largely unexplored. Therefore, a restricted singularity distribution which is constrained to generate a single closed slat is used in this semi-inverse solution.

Once the slat shape has been generated by the semi-inverse solution, the accuracy with which the specified flow field has been matched can be checked using an exact numerical solution technique

such as the Douglas-Neumann.

The flow solution for the slat and airfoil under off-design flight conditions can, in principle, be obtained, without solving a new integral equation, from the single inverse solution which generated the slat. The flow velocities along the airfoil and slat from the inverse solution can be integrated to obtain the potential at each point. Since the potential is also known along the two segments of the real axis which comprise the classical tandem biplane (6, p. 171), the potential to potential mapping can be determined. The slat and airfoil velocity distributions off the design point can then be obtained by using this mapping to transform the known tandem biplane solution for the appropriate angle of attack to the airfoil plane. This proposed transformation solution for the off-design flow appears to be shorter and to require less computer storage than the numerical integral equation solutions of the Douglas-Neumann type. However, the alternative solution is not developed in this thesis because optimized Douglas-Neumann-type computer codes are now so readily available.

For an arbitrary airfoil, Riemann's theorem guarantees the existence of a conformal mapping to a circle, and numerical techniques to determine the transformation have been developed. Thwaites (7, pp. 117, 125) discusses the general circle mapping and extensions of Theodorsen's exact solution for arbitrary airfoils. In this thesis, the circle mapping is assumed to be available. Because the solution for circulatory potential flow around a circle is well known, applying the inverse of the circle transformation

yields the inviscid velocity distribution on the airfoil without a slat.

The desirable pressure distribution on the airfoil is assumed to be known. For a specified airfoil and flight Reynolds number, the pressure gradient behind the minimum pressure point which the boundary layer can tolerate without separation can be estimated using one of the numerous separation criteria available in the literature.

In Boundary Layer and Flow Control, Cooke and Brebner (8) recommend the separation criteria of Thwaites and of Curle and Skan if the airfoil nose boundary layer is expected to be laminar, and suggest the turbulent separation criteria of Maskell or Spence downstream of the predicted transition point. Schlichting's analysis (9, p. 210) based on the Kármán-Pohlhausen approximation provides an estimate of the most severe deceleration history a laminar boundary layer can tolerate without separation. However, none of these separation prediction methods are generally accepted as accurate, and this paper makes no attempt to determine which is most appropriate for the nose boundary layer of a slatted airfoil. For a particular airfoil, it is assumed that a nose pressure distribution which is desirable according to some suitable criterion can be specified.

The difference between the known velocity on the unslatted airfoil nose and the velocity specified as desirable from boundary-layer considerations is defined as the specified modulating velocity. The semi-inverse design technique generates a slat whose induced velocity field on the airfoil closely matches this specified modulating

velocity distribution. An approximate matching of the specified modulating field is consistent with the approximations inherent in the semi-empirical boundary-layer separation criteria from which the specified velocity distribution is derived.

Using the circle mapping which is assumed to be known, the required modulating field on the circle can be obtained from the specified modulating velocity distribution on the airfoil. The semi-inverse problem of this thesis can then be posed in the following form. Determine a distribution of a restricted class of singularities outside the circle which will approximately match the specified modulating velocity field on the circle.

II. ANALYSIS

A. Basic Domains for the Solution

A brief initial description of the major steps in this semi-inverse slat design technique is appropriate.

The mapping to a circle for an arbitrary airfoil is assumed known. By introducing an additional conformal transformation from the circle to an ellipse of the same nose radius to chord ratio as the original airfoil, an alternate basic domain in which the nose flow has direct physical significance is obtained. Through a sequence of conformal transformations, the ellipse surface is mapped to the real axis of a half-plane in which the transformed ellipse nose is at the origin. At lift coefficients which are sufficiently high to require a slat, the near-surface streamlines of the ellipse plane flow from the lower stagnation point around the nose conform closely to the curvature of the ellipse. These nose streamlines transform to sloping lines of small curvature in the upper half-plane. The slat chord can then be approximated by an inclined straight line segment placed along one of these half-plane streamlines. Selection of the slat chord and location is based on the distribution of the transformed specified modulating velocity along the real axis of the half-plane.

Camber and thickness of the slat are represented by a finite series of distributed singularities on the slat chord line. The slat-induced velocity on the real axis can then be expressed in terms of the unknown series coefficients. To determine the coefficients, a linear least squares matching of the slat field to the specified modulating velocity distribution is used. On the slat chord line, the

normal velocities induced by the singularity distributions correspond to the sine and cosine camber and thickness modes of thin airfoil theory. The slat shape in the half plane is determined by integration of the linearized local flow inclination. Finally, the slat geometry in the ellipse plane is obtained by applying the inverse of the mapping to the half plane. Detailed discussions of each step of the analysis are given in the following sections.

The ellipse plane is an analytically convenient basic domain in which the nose flow closely models the operating flow environment of the slat. For most airfoils without extreme leading edge camber or nose droop, the nose is very nearly elliptical. Thus the airfoil to ellipse mapping is one-to-one in the nose region. Because leading edge slats and nose droop are alternative solutions for the problem of high nose velocities on thin airfoils, a highly cambered leading edge is not required on an airfoil intended to operate at high lift coefficients only with a nose slat extended.

The complex potential for a circle with circulation in a uniform onset flow is well known, and the streamline equation in the circle plane can be readily derived. When mapped to the ellipse plane, the streamline pattern provides a graphical visualization of the nose flow without a slat. Because the dominant parameters in the nose region are the total circulation and the nose radius, these streamlines around the ellipse nose will closely resemble the leading edge flow pattern for the original airfoil.

The Joukowski transformation

$$Z = z + \frac{c_7}{4z} \qquad c_7 \equiv a^2 - b^2$$

maps a circle of radius $c_3 \equiv (a + b)/2$ in the $z \equiv x_2 + iy_2$ plane into an ellipse of thickness ratio τ in the $Z = x_1 + iy_1$ plane. The semi-major axis of the ellipse is defined as a, and the semi-minor axis as b. The nose radius of the ellipse, $R_0 = a\tau^2$, can be normalized by the chord 2a:

$$\frac{R_0}{2a} = \frac{\tau^2}{2} \qquad \tau \equiv b/a$$

For large z, the mapping derivative $|dZ/dz|$ approaches unity as $1/z^2$, and the distant flow field is therefore the same in both planes.

B. Conformal Mappings Required for Semi-Inverse Solution

The initial step in the mapping to the half-plane from the ellipse plane Z is to return to the circle plane z by the inverse Joukowski transformation:

$$z = (1/2)\,(Z + \sqrt{Z^2 - c_7})$$

The flow external to the airfoil circle of radius c_3 is mapped to the upper half-plane $\mathcal{I}(W) \geq 0$ by the following bilinear transformation:

$$W = i\left(\frac{z+c_3}{z-c_3}\right) \qquad W \equiv x_3 + iy_3$$

This transformation sequence opens the ellipse at the trailing edge, unfolds it about the leading edge to a straight line, and, by a rotation

of $\pi/2$, maps the ellipse surface onto the real axis in the W plane with the nose at the origin. The ellipse trailing edge maps to infinity in the half-plane, and the circle at infinity in the ellipse plane collapses to the point W = +i. The upper and lower midchord points of the ellipse, ($x_1 = 0, y_1 = +b$) and ($x_1 = 0$, $y_1 = -b$), map to the points ($x_3 = +1$, $y_3 = 0$) and ($x_3 = -1$, $y_3 = 0$).

The nose region for the particular ellipse used as a test case in Part III is shown in Figure 2, and the transformations of this region into the circle plane and half-plane are given in Figures 3 and 4, respectively. Corresponding coordinate grids are plotted in each of the domains. Distortion of these grids during the transformations illustrates the variation of the mapping derivatives over the planes. The mapping of the concentric circles in the z plane into confocal ellipses in the Z plane is, of course, a classical property of the Joukowski transformation.

The circulation of the ellipse without a slat is fixed by prescribing zero velocity at the trailing edge ($x_1 = a$, $y_1 = 0$). For an ellipse of thickness ratio τ at an angle of attack α in a uniform onset flow with velocity U, this circulation Γ_0 required to satisfy the Kutta Condition is $\Gamma_0 = 4\pi U c_3 \sin\alpha$. The section lift coefficient C_ℓ is

$$C_\ell = 2\pi(1+\tau)\sin\alpha$$

As will be discussed in Section E, the addition of a leading edge slat of circulation Γ_s requires a small additional increment of compensating vorticity, Γ_c, on the ellipse to maintain the Kutta condition. The total circulation on the ellipse, Γ_t, is then given by

in that domain.

For the lifting ellipse without a slat, the total circulation Γ_t on the ellipse is the basic circulation Γ_0 required to establish the Kutta condition at the ellipse trailing edge. If the circle plane variable z is expressed in polar form as $z = re^{i\theta}$, then the scalar potential $\Phi(z) = \mathcal{R}[F(z)]$ and the stream function $\Psi(z) = \mathcal{I}[F(z)]$ are readily obtained from the complex potential.

$$F(z) = U\left\{re^{i(\theta-\alpha)} + (\frac{c_3^2}{r})e^{-i(\theta-\alpha)} + 2ic_3\sin\alpha \log[(\frac{r}{c_3})e^{i(\theta-\alpha)}]\right\}$$

$$F(z) = \Phi(z) + i\Psi(z)$$

$$\Phi(z) = U\left\{[r + (\frac{c_3^2}{r})]\ \cos(\theta-\alpha) - 2c_3(\theta-\alpha)\sin\alpha\right\}$$

$$\Psi(z) = U\left\{[r - (\frac{c_3^2}{r})]\ \sin(\theta-\alpha) + 2c_3\sin\alpha(\log r - \log c_3)\right\}$$

The last equation can be rewritten to express the azimuthal coordinate θ along the streamline Ψ as a function of the circle plane radial variable r.

$$\theta = \alpha + \sin^{-1}\left\{\left[\frac{2rc_3\sin\alpha}{c_3^2 - r^2}\right]\log(\frac{r}{c_3}) - \frac{\Psi}{U}(\frac{r}{c_3^2 - r^2})\right\}$$

The stagnation streamline is assigned $\Psi = 0$, and the argument of the front stagnation point in the circle plane is $\theta = \pi + 2\alpha$. The transformation to the Cartesian coordinates $W = x_3 + iy_3$ in the half-plane is

$$x_3 = \frac{2(\frac{c_3}{r})\sin\theta}{1 - 2(\frac{c_3}{r})\cos\theta + (\frac{c_3}{r})^2}; \quad y_3 = \frac{1 - (\frac{c_3}{r})^2}{1 - 2(\frac{c_3}{r})\cos\theta + (\frac{c_3}{r})^2}$$

Under this transformation, the nose stagnation point maps to

$$x_{3_s} = - \frac{\sin 2\alpha}{1+\cos 2\alpha}$$

In the same notation, the Joukowski transformation to the ellipse plane $Z = x_1 + iy_1$ is written as

$$x_1 = [r + (\frac{c_7}{4r})] \cos\theta; \qquad y_1 = [r - (\frac{c_7}{4r})] \sin\theta$$

Using a simple digital computer program, the streamline coordinates in the circle plane can be obtained by repeatedly evaluating the stream function equation given above. Equal increments of the stream function parameter Ψ are chosen so that the convergence of the streamlines is a consistent representation of local flow velocity increases. For a fixed value of Ψ, repeated solution of this equation for θ at closely spaced values of r across the appropriate range yields a set of (r, θ) coordinates along the streamline. The circle plane streamlines can then be mapped point by point to the ellipse plane Z and the half-plane W by employing the two transformations given above.

For the test case ellipse described in Part III, the streamlines around the ellipse nose are shown in Figure 2 and the flow pattern in the half-plane is shown in Figure 4. The uniform onset flow in the ellipse and circle planes collapses to an inclined vortex doublet at $W = +i$ in the half-plane. A small region above and to the right of the origin in the half-plane is the domain for effective slats. In this region, the mild curvature of the main flow streamlines permits the straight line segment representation of the slat

chord line. For slats close to the transformed ellipse nose surface, the inclination of the chord line will be small. However, the displacement of the slat chord line due to this inclination cannot be neglected in comparison to the slat height above the real axis. For slats farther from the ellipse nose, the chord line inclination in the half-plane can be large. The real axis is the line of symmetry for the W plane flow, and the flow system in the lower half-plane is a mirror image of the streamline pattern illustrated in Figure 4.

An additional transformation from the half-plane to the slat-centered half-plane or slat plane is introduced so that the expressions for the induced velocity field of the slat and the slat shape integration can be written in a general form independent of the slat geometry parameters. The four slat geometry parameters are defined in the half-plane as shown in Figure 5. The slat chord is defined as c_2; the height of the midchord point above the real axis and the lateral offset of this point from the imaginary axis are designated f_1 and f_2, respectively; and the angle between the slat chord and the real axis is defined as k_6.

As will be discussed in Part III, the slat chord, height, and offset are selected by examination of the distribution of specified modulating velocity along the real axis in the half-plane. The distributed singularities on the slat have characteristic induced velocity distributions on the transformed ellipse nose. Comparison of these characteristic slat-induced fields with the specified modulation field provides the insight required to select an effective slat location. Initially, the slat chord inclination k_6 is determined by prescribing

that the slat midchord be set parallel to the main flow velocity at that point. The deviation of the slat surfaces from the assumed position of the slat singularities along the chord line is initially taken to be negligible with respect to the slat height. Physically, this is a reasonable assumption, because an unstalled slat is limited to an effective angle of attack of approximately ten degrees. Furthermore, this approximation is consistent with the thin airfoil linearizations which will be subsequently introduced into the slat analysis. In Part III, a higher order correction to the slat inclination is introduced.

The transformations from the ellipse plane to the circle plane and half-plane are implicit functions of the ellipse nose radius. In contrast, the mapping from the half-plane W to the slat plane $S \equiv s + it$ is a function of the slat geometry parameters only:

$$S = \left(\frac{4}{c_2}\right) e^{+ik_6} \left[W - (f_2 + if_1)\right]$$

This mapping translates the slat midchord to the S plane origin, rotates the entire plane by k_6 to place the slat chord along the $\mathcal{R}(S)$ axis, and uniformly dilates figures in the half-plane by the factor $(4/c_2)$.

The normal and parallel components of the main flow velocity along the slat chord ($-2 \leq s \leq 2$, $t = 0$) can be obtained by substituting the inverse slat plane mapping

$$W = \left(\frac{c_2 e^{-ik_6}}{4}\right) S + f_2 + if_1$$

into the equation for the complex potential F(W) on page 14.

The quantities D and E are defined as

$$D(S) \equiv W + i = \left(\frac{c_2 e^{-ik_6}}{4}\right) S + f_2 + i(f_1 + 1)$$

$$E(S) \equiv W - i = \left(\frac{c_2 e^{-ik_6}}{4}\right) S + f_2 + i(f_1 - 1)$$

The complex potential F(S) for the main flow in the slat plane is then given by

$$F(S) = Uc_3 \left[\left(\frac{D}{E}\right) e^{-i\alpha} + \left(\frac{E}{D}\right) e^{+i\alpha} \right] + i\left(\frac{\Gamma_t}{2\pi}\right)(\log D - \log E) + \alpha\left(\frac{\Gamma_t}{2\pi}\right)$$

Differentiation to obtain the complex velocity $\bar{q} = dF(S)/dS$ yields

$$\bar{q}(S) = D' \left\{ 2Uc_3 \left[\left(\frac{-i}{E^2}\right) e^{-i\alpha} + \left(\frac{i}{D^2}\right) e^{+i\alpha} \right] + \left(\frac{\Gamma_t}{\pi DE}\right) \right\}$$

$$D' \equiv \frac{dD}{dS} = \left(\frac{c_2}{4}\right) e^{-ik_6} = E'$$

Along the slat chord, S = s, and a sequence of intermediate variables can be defined as follows.

$$k_7 \equiv \cos k_6 \qquad k_8 \equiv \sin k_6$$

$$D(s) = \left[\left(\frac{c_2}{4}\right) k_7 s + f_2 \right] + i \left[f_1 - \left(\frac{c_2}{4}\right) k_8 s + 1 \right] \equiv f_3 + i f_4$$

$$E(s) = \left[\left(\frac{c_2}{4}\right) k_7 s + f_2 \right] + i \left[f_1 - \left(\frac{c_2}{4}\right) k_8 s - 1 \right] \equiv f_3 + i f_5$$

$$D^2 \equiv f_6 + i f_7 = f_3^2 - f_4^2 + i(2 f_3 f_4)$$

$$E^2 \equiv f_8 + if_9 = f_3^2 - f_5^2 + i(2f_3f_5)$$

$$DE \equiv f_{12} + if_{13} = f_3^2 - f_4f_5 + i(f_3f_4 + f_3f_5)$$

$$\frac{1}{D^2} = \frac{f_6 - i f_7}{f_{14}} \; ; \; f_{14} \equiv f_6^2 + f_7^2$$

$$\frac{1}{E^2} = \frac{f_8 - if_9}{f_{15}} \; ; \; f_{15} \equiv f_8^2 + f_9^2$$

$$\frac{1}{DE} = \frac{f_{12} - if_{13}}{f_{16}} \; ; \; f_{16} \equiv f_{12}^2 + f_{13}^2$$

$$k_2 \equiv \alpha - k_6 \; ; \; k_{12} \equiv \cos k_2 \; ; \; k_{13} \equiv \sin k_2$$

$$k_3 \equiv \alpha - k_6 \; ; \; k_{14} \equiv \cos k_3 \; ; \; k_{15} \equiv \sin k_3$$

$$c_4 \equiv \frac{Uc_2c_3}{2f_{14}} \; ; \; c_5 \equiv \frac{Uc_2c_3}{2f_{15}} \; ; \; c_6 \equiv \frac{c_2\Gamma_t}{4\pi f_{16}}$$

In terms of these intermediate variables, the complex velocity is

$$\bar{q}(s) = c_4[f_7k_{12} - f_6k_{13} + i(f_6k_{12} + f_7k_{13})]$$

$$- c_5[f_9k_{14} + f_8k_{15} + i(f_8k_{14} - f_9k_{15})]$$

$$+ c_6[f_{12}k_7 - f_{13}k_8 - i(f_{13}k_7 + f_{12}k_8)]$$

$$\bar{q}(s) \equiv c_4(f_{17} + if_{18}) - c_5(f_{19} + if_{20}) + c_6(f_{21} - if_{22})$$

At the slat chord station s_i, the parallel component of the main flow is designated u_{i20} and the component normal to the slat

is designated v_{i20}.

$$\overline{q}(s_i) \equiv u_{i20} - iv_{i20}$$

$$u_{i20} \equiv c_4 f_{17} - c_5 f_{19} + c_6 f_{21}$$

$$v_{i20} = -c_4 f_{18} + c_5 f_{20} + c_6 f_{22}$$

C. The Distributed Slat Singularities

The choice of a singularity representation for the slat is constrained by the requirements of other sections of the complete semi-inverse solution. An explicit expression for the slat-induced velocity field in terms of a finite series of singularity distribution mode coefficients is needed. The inversion can then be conducted using a least squares technique to select the coefficients required to match the specified modulation field. Furthermore, the local flow field along the slat chord line must be continuous to permit integration of the local flow slopes to obtain the slat shape. A distributed singularity representation rather than a multiple point vortex model is therefore required.

The complex velocity functions employed in this solution can be derived by a further Joukowski transformation $S = \zeta + 1/\zeta$ between the slat circle plane ζ and the slat plane $S = s + it$ in which the slat chord is the portion of the real axis $-2 \leq s \leq 2$. Because the main flow is regular and singularities are added only along the slat chord, the velocity field outside the slat circle $|\zeta| = 1$ is free of singularities and can be represented by a Laurent's series $1/\zeta^n$.

After adding a term $1/(\zeta+1)$ which is singular at the point $\zeta = -1$ corresponding to the slat leading edge, the complex conjugate velocity in the slat circle plane can be written as the following finite series with real coefficients:

$$\overline{q}(\zeta) = (a_0 + ib_0)\left(\frac{1}{\zeta+1}\right) + \sum_{n=1} \left[(a_n + ib_n)\left(\frac{1}{\zeta^n}\right)\right]$$

The complex conjugate velocity is mapped back to the slat plane using the inverse Joukowski transformation.

$$\zeta = \frac{S + \sqrt{S^2-4}}{2}$$

The regular terms can then be written as

$$(a_n + ib_n)\left(\frac{1}{\zeta^n}\right) = (a_n + ib_n)\left(\frac{S-\sqrt{S^2-4}}{2}\right)^n \qquad n > 0$$

and the singular terms have the following form:

$$(a_0 + ib_0)\left(\frac{1}{\zeta+1}\right) = (a_0 + ib_0)\left(1 - \sqrt{\frac{S-2}{S+2}}\right)$$

The a_n terms are source-sink distributions corresponding to slat thickness, and the b_n terms are vorticity distributions corresponding to slat camber. To satisfy the requirement that there be no net mass flux at infinity (a necessary condition for a closed slat), the two leading order thickness terms a_0 and a_1 must cancel as $S \to \infty$. Because $\zeta \to S$ as $S \to \infty$ and these two terms are $a_0/(\zeta+1)$ and a_1/ζ in the slat circle plane, it is apparent that closure requires $a_1 = -a_0$. As will be shown in the discussion of the slat shape modes corresponding to these singularity distributions, the singular a_0

term produces the finite slat nose radius and thus is chosen as positive.

The contribution to the induced velocity field by each of the distributed singularity modes on the slat can be evaluated along the transformed ellipse nose surface which is defined as the ground plane. The slat plane ordinates $S_i = s_i + it_i$ along this ground plane which correspond to each half-plane matching station $W = x_{i3} \equiv h_i$ are obtained from the slat plane transformation given below. In addition to the four slat geometry parameters (chord c_2, height f_1, offset f_2, angle k_6), the quantities $k_7 \equiv \cos k_6$ and $k_8 \equiv \sin k_6$ are utilized.

$$S = (4/c_2)\, e^{ik_6} \left[W-(f_2+if_1)\right] = (4/c_2)\, e^{ik_6} \left[(h_i-f_2)-if_1\right]$$

$$t_i = (4/c_2)\left[(h_i-f_2)k_8-f_1k_7\right];\quad s_i = (4/c_2)\left[(h_i-f_2)k_7+f_1k_8\right]$$

The uniform rotation under this transformation maps the $\mathcal{R}(W)$ axis onto the ground plane, a line with positive slope k_6. On this inclined ground plane below the slat, the parallel unit vector is $G = k_7 + ik_8$, and the unit normal vector directed away from the slat is $N = k_8 - ik_7$.

Because the complex <u>velocity</u> is conserved in the mapping between the slat plane and the slat circle plane, the regular complex conjugate velocity terms which are of the form

$$\overline{q}_n = (a_n + ib_n)\left(\frac{1}{\zeta^n}\right) \qquad n > 0$$

can be initially evaluated in the ζ plane. By defining the slat circle plane variable in polar form, $\zeta \equiv r_1 e^{i\phi_1}$, expressions for the $\overline{q}_n$ can

be obtained in terms of powers of the modulus r_1 and multiples of the polar angle ϕ_1.

$$\bar{q}_n = (a_n + ib_n)\left(\frac{1}{r_1^n}\right) e^{-i\phi_1}$$

$$\bar{q}_n = \left(\frac{1}{r_1^n}\right)\left[(a_n \cos n\phi_1 + b_n \sin n\phi_1) + i(b_n \cos n\phi_1 - a_n \sin n\phi_1)\right]$$

The velocity component u_n parallel to the transformed ellipse nose surface is obtained from the scalar product of $\bar{q}_n$ and the complex conjugate of the ground plane unit vector, $\bar{G}$.

$$u_n \equiv \bar{q}_n \cdot (k_7 - ik_8)$$

$$u_n = \left(\frac{1}{r_1^n}\right)\left[a_n(k_7 \cos n\phi_1 + k_8 \sin n\phi_1) + b_n(k_7 \sin n\phi_1 - k_8 \cos n\phi_1)\right]$$

For the singular camber and thickness terms, the induced flow component, u_0, parallel to the ground plane is obtained in the same manner.

$$(\zeta + 1) \equiv r_2 e^{i\phi_2}$$

$$\bar{q}_0 \equiv (a_0 + ib_0)\left(\frac{1}{\zeta+1}\right) = (a_0 + ib_0)\left(\frac{1}{r_2}\right) e^{-i\phi_2}$$

$$u_0 = \left(\frac{a_0}{r_2}\right)(k_7 \cos\phi_2 + k_8 \sin\phi_2) + \left(\frac{b_0}{r_2}\right)(k_7 \sin\phi_2 - k_8 \cos\phi_2)$$

Along the ground plane which is the axis of symmetry of the slat plane, the normal components of the velocity fields induced by the slat and by the image slat sum to zero. However, in the course of the evaluation of the velocity field induced on the slat by the image slat in Section F, the normal velocity components v_n are

required. The scalar product of $\overline{q}_n$ and the complex conjugate of the unit normal vector $\overline{N}$ is defined as v_n.

$$v_n \equiv \overline{q}_n \cdot \overline{N} = \overline{q}_n \cdot (k_8 + ik_7)$$

Comparing this equation for v_n with the basic expression for u_n given above, it is apparent that each of the normal components v_n can be obtained from the corresponding expression for u_n by substituting k_8 for k_7 and $-k_7$ for k_8. The geometrical variables r_1, r_2, ϕ_1 and ϕ_2 are expressed as functions of the slat plane coordinates $S = s + it$ through the inverse Joukowski transformation.

$$\zeta = \frac{S+\sqrt{S^2-4}}{2}$$

A double subscript notation r_{i1}, r_{i2}, etc. is introduced to identify values of the geometrical variables with their associated matching station h_i in the half-plane.

Several intermediate variables are introduced during the evaluation of the primary geometrical variables which is given below. In this notation, the slat circle plane variable is

$$\zeta_i = (\tfrac{1}{2})\left\{s_i + it_i + \left[(s_i + it_i)^2 - 4\right]^{\frac{1}{2}}\right\}$$

If the square root term is written in polar form,

$$r_{i3}e^{2i\phi_{i3}} \equiv (s_i + it_i)^2 - 4$$

then ζ_i can be expressed as

$$\zeta_i = (\tfrac{1}{2})\left\{s_i + it_i + \left[r_{i3}e^{2i\phi_{i3}}\right]^{\frac{1}{2}}\right\}$$

The intermediate variable $p_{i5} \equiv \sin 2\phi_{i3}$ is utilized in the evaluation of the real and imaginary components of the square root term which are defined as r_{i4} and r_{i5} respectively.

$$r_{i3} = \left[s_i^4 + t_i^4 + 8(t_i^2 - s_i^2) + 2s_i^2 t_i^2 + 16\right]^{\frac{1}{2}}$$

$$p_{i5} \equiv \sin 2\phi_{i3} = \frac{2s_i t_i}{r_{i3}} \qquad \cos 2\phi_{i3} = \frac{s_i^2 - t_i^2 - 4}{r_{i3}}$$

$$r_{i4} \equiv (r_{i3})^{\frac{1}{2}} \sin\phi_{i3} = \left[(\tfrac{1}{2})(r_{i3} - s_i^2 + t_i^2 + 4)\right]^{\frac{1}{2}}$$

$$r_{i4} = -\left[\qquad\qquad\right]^{\frac{1}{2}} \quad \underline{\text{if}}\ s_i < 0\ \ \underline{\text{or}}\ p_{i5} < 0$$

$$r_{i5} \equiv (r_{i3})^{\frac{1}{2}} \cos\phi_{i3} = \left[(\tfrac{1}{2})(r_{i3} + s_i^2 - t_i^2 - 4)\right]^{\frac{1}{2}}$$

$$r_{i5} = -\left[\qquad\qquad\right]^{\frac{1}{2}} \quad \underline{\text{if}}\ p_{i5} > 0\ \ \underline{\text{and}}\ \ s_i < 0$$

By equating the Cartesian expression for ζ_i

$$\zeta_i = (\tfrac{1}{2})\left[(s_i + r_{i5}) + i(t_i + r_{i4})\right]$$

with the polar form

$$\zeta_i = r_{il} \exp(i\phi_{il}) \equiv r_{il}(p_{il} + ip_{i2})$$

the modulus r_{il} and the two geometrical variables $p_{il} \equiv \cos\phi_{il}$ and $p_{i2} \equiv \sin\phi_{il}$ can be evaluated.

$$r_{il} = (\tfrac{1}{2})\left[(s_i + r_{i5})^2 + (t_i + r_{i4})^2\right]^{\frac{1}{2}}$$

$$p_{il} = \frac{s_i + r_{i5}}{2r_{il}} \qquad p_{i2} = \frac{t_i + r_{i4}}{2r_{il}}$$

The quantity $(\zeta_i + 1) \equiv r_{i2} \exp(i\phi_{i2})$ which appears in the singular velocity functions can be similarly expressed in terms of the modulus r_{i2} and two additional geometrical variables, $p_{i3} \equiv \cos\phi_{i2}$ and $p_{i4} \equiv \sin\phi_{i2}$.

$$(\zeta_i+1) \equiv r_{i2}(p_{i3} + ip_{i4}) = r_{i1}(p_{i1} + ip_{i2}) + 1$$

$$r_{i2} = (r_{i1}^2 + 2r_{i1}p_{i1} + 1)^{\frac{1}{2}}$$

$$p_{i3} = \frac{r_{i1}\, p_{i1} + 1}{r_{i2}} \quad ; \qquad p_{i4} = \frac{r_{i1} p_{i2}}{r_{i2}}$$

For this semi-inverse solution, the eight highest order complex velocity functions are used to represent the slat thickness and camber modes required to match the specified velocity distribution. All of the coefficients are redesignated as B_I. The first four camber terms are designated B_1, B_2, B_3, and B_4; the primary thickness mode B_5 is the singular a_0 term minus the first regular thickness term a_1; and the second and third regular thickness terms are redesignated as B_6 and B_7. These seven complex conjugate velocity functions q_I are defined below as functions of the slat plane variable S. The signs are chosen so that a positive coefficient B_I corresponds to positive camber or thickness on the forward part of the slat. (10)

$$\underline{\text{singular camber mode } B_1}$$

$$\overline{q}_1 \equiv \frac{iB_1}{2}\left[1 - \left(\frac{S-2}{S+2}\right)^{\frac{1}{2}}\right]$$

first regular camber mode B_2

$$\bar{q}_2 \equiv \frac{iB_2}{2}\left[S-(S^2-4)^{\frac{1}{2}}\right]$$

second regular camber mode B_3

$$\bar{q}_3 \equiv \frac{-iB_3}{2}\left[S^2-S(S^2-4)^{\frac{1}{2}}-2\right]$$

third regular camber mode B_4

$$\bar{q}_4 \equiv iB_4\left[\frac{S-(S^2-4)^{\frac{1}{2}}}{2}\right]^3$$

primary thickness mode B_5

$$\bar{q}_5 \equiv \frac{B_5}{2}\left\{\left[1-\left(\frac{S-2}{S+2}\right)^{\frac{1}{2}}\right]-\left[S-(S^2-4)^{\frac{1}{2}}\right]\right\}$$

second regular thickness mode B_6

$$\bar{q}_6 \equiv \frac{-B_6}{2}\left[S^2-S(S^2-4)^{\frac{1}{2}}-2\right]$$

third regular thickness mode B_7

$$\bar{q}_7 \equiv B_7\left[\frac{S-(S^2-4)^{\frac{1}{2}}}{2}\right]^3$$

The influence coefficients u_{iI} for these seven singularity distribution modes are the basic input for the linear least squares solution which is used to select the mode coefficients B_I required to match the specified modulating velocity field. The influence coefficient u_{iI} is defined as the velocity component parallel to the ground plane (at the slat plane coordinates (s_i, t_i) corresponding to

the matching station h_i) which would be induced by the I^{th} singularity distribution mode with coefficient B_I of unity. By selecting the appropriate terms from the general induced field expressions given on page 24 and applying the multiple angle formulas, the seven influence coefficient functions can be expressed in terms of the six basic geometrical variables r_{i1}, r_{i2}, p_{i1}, p_{i2}, p_{i3}, and p_{i4} as defined on pages 26 and 27.

Influence Coefficients u_{il}

singular camber mode B_1

$$u_{i1} = \left(\frac{1}{r_{i2}}\right)(k_7 p_{i4} - k_8 p_{i3})$$

first regular camber mode B_2

$$u_{i2} = \left(\frac{1}{r_{i1}}\right)(k_7 p_{i2} - k_8 p_{i1})$$

second regular camber mode B_3

$$u_{i3} = \left(\frac{-1}{r_{i1}^2}\right)(k_7 \sin 2\phi_1 - k_8 \cos 2\phi_1)$$

$$u_{i3} = \left(\frac{-1}{r_{i1}^2}\right)\left[2k_7 p_{i1} p_{i2} - k_8 (p_{i1}^2 - p_{i2}^2)\right]$$

third regular camber mode B_4

$$u_{i4} = \left(\frac{1}{r_{i1}^3}\right)(k_7 \sin 3\phi_1 - k_8 \cos 3\phi_1)$$

$$u_{i4} = \left(\frac{1}{r_{i1}^3}\right)\left[k_7 (3p_{i2} - 4p_{i2}^3) - k_8 (4p_{i1}^3 - 3p_{i1})\right]$$

primary thickness mode B_5

$$u_{i5} = \left(\frac{1}{r_{i2}}\right)(k_7 p_{i3} + k_8 p_{i4}) - \left(\frac{1}{r_{i1}}\right)(k_7 p_{i1} + k_8 p_{i2})$$

second regular thickness mode B_6

$$u_{i6} = \left(\frac{-1}{r_{i1}^2}\right)(k_7 \cos 2\phi_1 + k_8 \sin 2\phi_1)$$

$$u_{i6} = \left(\frac{-1}{r_{i1}^2}\right)\left[k_7(p_{i1}^2 - p_{i2}^2) + 2k_8 p_{i1} p_{i2}\right]$$

third regular thickness mode B_7

$$u_{i7} = \left(\frac{1}{r_{i1}^3}\right)(k_7 \cos 3\phi_1 + k_8 \sin 3\phi_1)$$

$$u_{i7} = \left(\frac{1}{r_{i1}^3}\right)\left[k_7(4p_{i1}^3 - 3p_{i1}) + k_8(3p_{i2} - 4p_{i2}^3)\right]$$

The slat plane flow is symmetric about the ground plane since the uniform translation, rotation, and dilatation during the mapping to the slat plane do not impair the half-plane's symmetry above and below the real axis. The induced velocity field of the image slat therefore doubles the slat-induced parallel flow component along the ground plane and cancels the normal component of the slat field. Thus the parallel velocity component q_{iI} induced by the I^{th} singularity mode at the matching station h_i in the half-plane is twice the product of the mode coefficient B_I, the slat plane to half-plane mapping derivative $4/c_2$, and the influence coefficient u_{iI}:

$$\text{at } x_{i3} = h_i, \quad q_{iI} \equiv B_I(8/c_2)u_{iI} \quad \text{for} \quad I = 1, 2, \ldots, 7$$

The influence coefficients for a slat of zero inclination at height-to-chord ratios of one, one-half, and one-quarter are shown in Figures 6A, 6B, and 6C. The influence coefficients for a slat at a height-to-chord ratio of unity with an inclination of $\pi/4$ are illustrated in Figure 6D.

Along the slat chord line which is the segment $(-2 \leq s \leq 2, t = 0)$ of the slat plane real axis, the chordwise station can be defined in terms of the argument θ as $s = 2\cos(\theta)$. The regular complex velocity expressions from pages 27 and 28 are then reduced to the classical Fourier modes $\cos(n\theta)$ and $\sin(n\theta)$ of thin airfoil theory, and the singular terms have a $\tan(\theta/2)$ dependence. This formulation of the local velocity field on the slat chord simplifies the final integration for the slat shape. The normal flow components induced by the camber modes are symmetric above and below the chord line, and the parallel u components are antisymmetric. For the thickness modes, the v components are antisymmetric and the u components are symmetric. The signs given below for the seven sets of parallel and normal velocity components induced by the singularity distribution modes are those appropriate to the top surface of the slat chord line at the station $s_i = 2\cos(\theta_i)$.

<u>singular camber mode B_1</u>

$$v_{il1} \equiv -\frac{B_1}{2} \qquad u_{il1} \equiv \left(\frac{B_1}{2}\right) \tan\left(\frac{\theta_i}{2}\right)$$

<u>first regular camber mode B_2</u>

$$v_{il2} \equiv -B_2 \cos\theta_i \qquad u_{il2} \equiv B_2 \sin\theta_i$$

second regular camber mode B_3

$$v_{il3} \equiv B_3 \cos 2\theta_i \quad u_{il3} \equiv -B_3 \sin 2\theta_i$$

third regular camber mode B_4

$$v_{il4} \equiv -B_4 \cos 3\theta_i \quad u_{il4} \equiv B_4 \sin 3\theta_i$$

primary thickness mode B_5

$$v_{il5} \equiv \left(\frac{B_5}{2}\right)\left[\tan\left(\frac{\theta_i}{2}\right) - 2 \sin \theta_i\right] \quad u_{il5} \equiv \left(\frac{B_5}{2}\right)(1-2 \cos \theta_i)$$

second regular thickness B_6

$$v_{il6} \equiv -B_6 \sin 2\theta_i \quad u_{il6} \equiv -B_6 \cos 2\theta_i$$

third regular thickness B_7

$$v_{il7} \equiv B_7 \sin 3\theta_i \quad u_{il7} \equiv B_7 \cos 3\theta_i$$

The slat circulation Γ_s is obtained by integrating the local vorticity $\gamma(s)$ along the slat chord. Applying the thin airfoil linearization, the local vorticity is twice the camber-induced parallel velocity component on the slat chord line. The contributions Γ_I to the slat circulation by the four camber modes are evaluated below.

regular camber modes $I = 2, 3, 4$

$$\Gamma_I = \int_{\text{L. E.}}^{\text{T. E.}} \gamma_I(s)ds = 2\int_{-2}^{+2} u_I(s)ds = 4\int_0^{\pi} u_I(\theta)\sin\theta\, d\theta$$

$$= 4B_I \int_0^{\pi} \sin\left[(I-1)\theta\right] \sin\theta\, d\theta = 2\pi B_2 \quad \text{for } I = 2$$

$$= 0 \text{ for } I = 3, 4$$

singular camber mode I = 1

$$\Gamma_1 = 2B_1 \int_0^{\pi} \tan(\frac{\theta}{2})\sin\theta \, d\theta = 2B_1 \int_0^{\pi} [\frac{1-\cos\theta}{\sin\theta}]\sin\theta \, d\theta = 2\pi B_1$$

The total slat circulation is then $\Gamma_s = 2\pi(B_1+B_2)$. Without altering the total circulation, the second and third regular camber modes redistribute vorticity along the slat chord.

D. Linear Least Squares Solution for Slat Mode Coefficients

Higher order slat singularity distribution modes which could introduce undesirable waviness in the slat surface and sharp local fluctuations in the induced velocity on the ellipse nose have been excluded. The four camber and three thickness modes employed in this solution provide seven coefficients to be selected to match the slat-induced velocity w_{i1} to the specified modulating velocity w_{i2} at the matching stations h_i in the half-plane. For a particular slat geometry (slat chord, height, offset, and angle fixed), the total slat-induced field at h_i is a linear function of the mode coefficients B_I. $w_{i1} \equiv \sum_{I=1}^{7} q_{iI}$

$$w_{i1} = (\frac{8}{c_2})(B_1 u_{i1} + B_2 u_{i2} + \ldots + B_7 u_{i7}) \quad \text{for} \quad i = 1, \ldots, e$$

The total number of matching stations is designated e. A linear least squares technique (11) is used to solve the following system of e linear equations

$$w_{i2} = (\frac{8}{c_2})(B_1 u_{i1} + B_2 u_{i2} + \ldots\ldots + B_7 u_{i7}) \quad \text{for} \quad i = 1, \ldots, e$$

for an arbitrarily large number of matching stations.

Although the regular velocity functions are mutually orthogonal on the slat chord, their induced fields on the inclined ground plane below the slat are not.

The linear least squares technique is employed to select the set of coefficients which minimizes the sum ϕ of the squares of the differences δ_i between the specified and slat-induced velocities at the matching stations.

$$\delta_i \equiv (w_{i2} - w_{i1})(\frac{c_2}{8})$$

$$\delta_i = (\frac{c_2}{8})\, w_{i2} - (B_1 u_{i1} + B_2 u_{i2} + \ldots + B_7 u_{i7})$$

$$\phi \equiv \sum_{i=1}^{e} \delta_i^2$$

Differentiation with respect to B_I to satisfy the minimization condition

$$0 = (\frac{-1}{2})\frac{\partial \phi}{\partial B_I} \quad \text{for} \quad I = 1, \ldots, 7$$

generates the seven normal equations

$$0 = \sum_{i=1}^{e} u_{iI}\delta_i \quad \text{for} \quad I = 1, \ldots, 7$$

The normal equations can be rewritten in matrix form by defining the (e by 7) influence coefficient matrix U, the 7-element vector of mode coefficients β, and the e element vectors of specified modulating velocities ω and of differences δ.

$$U \equiv \begin{bmatrix} u_{11} \cdots u_{17} \\ \vdots \\ u_{e1} \cdots u_{eT} \end{bmatrix}; \quad \beta \equiv \begin{bmatrix} B_1 \\ \vdots \\ B_7 \end{bmatrix}; \quad \omega \equiv \left(\frac{c_2}{8}\right) \begin{bmatrix} w_{12} \\ \vdots \\ w_{e2} \end{bmatrix}; \quad \delta \equiv \begin{bmatrix} \delta_1 \\ \vdots \\ \delta_e \end{bmatrix}$$

$$0 = U^T \delta$$

$$0 = U^T(\omega - U\beta)$$

$$U^T U\beta = U^T \omega$$

The relatively small 7 x 7 influence coefficient product matrix $A \equiv U^T U$ can be readily inverted using a standard digital computer subroutine, and the mode coefficient solution vector β is then obtained by a final matrix multiplication, $\beta = A^{-1} U^T \omega$.

E. Maintaining the Kutta Condition on Ellipse when Slat is Added

When a leading edge slat of circulation Γ_s is added near the nose of the ellipse, the vorticity of the image slat $\Gamma_i = -\Gamma_s$ is subtracted from the circulation of the ellipse. Because the image slat's negative vorticity is closer to the ellipse trailing edge than the vorticity on the slat itself, a small backflow or upward net velocity is induced at the trailing edge. An increment of compensating vorticity Γ_c at the ellipse center is therefore required to restore the Kutta Condition by cancelling this backflow.

Consider the elementary case of a point vortex on the centerline ahead of a circle of radius R. The total vertical velocity at the trailing edge $V_{T.E.}$ is the sum of the contributions from the slat vortex at radius κ, the image vortex at radius R^2/κ, and the

compensating vortex at the center of the circle.

$$V_{T.E.} = \frac{\Gamma_s}{2\pi(\kappa+R)} - \frac{\Gamma_s}{2\pi(\frac{R^2}{\kappa}+R)} + \frac{\Gamma_c}{2\pi R}$$

Because the Kutta Condition requires $V_{T.E.} = 0$, the compensating vorticity for this trivial case is

$$\Gamma_c = (\frac{\kappa-R}{\kappa+R})\,\Gamma_s$$

For realistically thin ellipses and efficient slats of small standoff from the nose, the compensating vorticity Γ_c ranges from approximately 3 percent to .5 percent of the basic ellipse circulation Γ_0.

In the far field, the vorticity distributions on the slat can be represented by two point vortices. Returning briefly to the slat circle plane variable ζ, the B_1 and B_2 camber terms which have $1/\zeta$ dependence rapidly dominate the B_3 and B_4 terms which are attenuated as $1/\zeta^2$ and $1/\zeta^3$, respectively. For the far field, the singular or flat plate camber mode B_1 can thus be represented by a point vortex of circulation $2\pi B_1$ at the slat quarter-chord point, and the first regular camber mode B_2 can be represented by a second substitution vortex of strength $2\pi B_2$ located at the slat midchord.

The compensating vorticity required for each of these two substitution vortices can be readily determined in the circle plane. The geometrical variables are defined as shown schematically in Figure 7. A vortex of circulation Γ_{13} at the circle plane coordinates (x_{13}, y_{13}) induces a negative vertical velocity component V_s at the trailing edge.

$$V_s = \left(\frac{\Gamma_{13}}{2\pi r_{15}}\right) \cos\phi_s$$

$$V_s = \left(\frac{\Gamma_{13}}{2\pi}\right) \left(\frac{c_3 - x_{13}}{r_{15}^2}\right)$$

$$r_{15} \equiv \left[(c_3 - x_{13})^2 + y_{13}^2\right]^{\frac{1}{2}}$$

The primary vortex is at the radius $r_{13} = \left[x_{13}^2 + y_{13}^2\right]^{\frac{1}{2}}$, and the radial coordinate of the image vortex is $r_{14} = c_3^2/r_{13}$.

$$x_{14} = r_{14} \cos\theta_s = \frac{r_{14} x_{13}}{r_{13}} \quad ; \quad r_{16} \equiv \left[(c_3 - x_{14})^2 + y_{14}^2\right]^{\frac{1}{2}}$$

At the trailing edge of the circle, the positive vertical velocity component that the image vortex induces is given by

$$V_i = \left(\frac{-\Gamma_{13}}{2\pi r_{16}}\right) \cos\phi_i = \left(\frac{-\Gamma_{13}}{2\pi}\right) \left(\frac{c_3 - x_{14}}{r_{16}^2}\right)$$

The compensating vortex at the circle center must induce a vertical velocity V_c equal in magnitude and opposite in sign to the sum of the velocities induced by the substitution vortex and its image.

$$V_c = \frac{\Gamma_c}{2\pi c_3} = -(V_s + V_i)$$

$$\Gamma_c = c_3 \Gamma_{13} \left[\left(\frac{c_3 - x_{14}}{r_{16}^2}\right) - \left(\frac{c_3 - x_{13}}{r_{15}^2}\right)\right]$$

The half-plane coordinates of the slat midchord are, by definition ($x_3 = f_2$, $y_3 = f_1$), and the quarter chord coordinates are

$$x_3 = \left[f_2 - \left(\frac{c_2}{4}\right) \cos k_6 \right] ; \quad y_3 = \left[f_1 + \left(\frac{c_2}{4}\right) \sin k_6 \right]$$

By applying the half-plane to circle plane transformation given in Section G to these half-plane coordinates for the slat mid-chord and quarter chord points, the corresponding circle plane coordinates (x_2, y_2) for the two points can be determined. The total compensating vorticity required is the sum of the two values Γ_{c_1}, Γ_{c_2} obtained from the analysis above by successively designating Γ_{13} as $2\pi B_1$ and $2\pi B_2$ with the substitution vortex coordinates (x_{13}, y_{13}) set equal to $(x_2, y_2)_{1/4 \text{ chord}}$ and $(x_2, y_2)_{1/2 \text{ chord}}$, respectively.

F. Determination of the Slat Shape Corresponding to the Singularity Distribution

The exact streamline pattern for the flow around the distributed singularities on the slat chord line can, in principle, be determined. The main flow stream function in the half-plane is given in Section B, and the stream functions for the slat and image slat singularity distributions can be obtained by integration of the expressions for the complex velocity fields which are given in Section C. However, a closed slat surface streamline encompassing all of the singularities may not exist. Near the cusped slat trailing edge, singularities will generally lie outside of the slat surface streamline. In that region, the non-zero normal flow components due to the slight curvature of the main flow field, the image slat field, and the vorticity on the chord line will all distort the slat surface streamline away from the line of singularities.

Furthermore, a lengthy non-linear solution for the slat shape is inconsistent with other inherent approximations in this semi-inverse design technique. A linearized integration is therefore used to determine the slat ordinates in the slat plane. The distortion of the slat due to the mild curvature of the main flow field and the field of the image slat are approximately taken into account.

Initially neglecting both the slight curvature of the main flow field in the slat plane and the velocity field induced by the image slat, the parallel flow component along the slat chord, u_{22}, is assumed to be constant. The accuracy of this approximation is discussed later in the section. Assuming this uniform onset flow and applying the linearizations of thin airfoil theory, the basic mean line and fairing shapes which correspond in the slat plane to the seven singularity distributions on the slat chord can be determined by integration in closed form. The linearized tangential flow boundary condition is used, and the slope dt/ds of the slat surface at the chord station $s_i = 2 \cos(\theta_i)$ is then given by

$$\left(\frac{dt}{ds}\right)_i = \frac{v_{i22}}{u_{22}}$$

In this expression, v_{i22} is the total normal velocity component evaluated at s_i on the chord line. The ordinates t_i of the upper and lower slat surfaces are designated as y_{i6} and y_{i7}, respectively. Integrating forward from the trailing edge where the ordinates are defined as zero, the upper surface ordinate at s_i is

$$y_{i6} = \int_{+2}^{s_i} \left[\frac{dt}{ds}\right] ds = \int_{0}^{\theta_i} \left[\frac{dt(\theta)}{ds}\right] \left(\frac{ds}{d\theta}\right) d\theta = \left(\frac{-2}{u_{22}}\right) \int_{0}^{\theta_i} \left[v_{i22}(\theta) \sin\theta\right] d\theta$$

The sum of the normal velocities induced by the four camber singularity distributions, B_1, B_2, B_3, and B_4 is designated v_{il0} and is symmetric above and below the chord line.

$$v_{il0} \equiv v_{il1} + v_{il2} + v_{il3} + v_{il4}$$

The contribution to the self-induced normal velocity by the three thickness modes B_5, B_6, and B_7 is designated v_{il8} and is antisymmetric.

$$v_{il8} \equiv v_{il5} + v_{il6} + v_{il7}$$

Along the upper slat surface, the total self-induced normal velocity is therefore $v_{il0} + v_{il8}$, and on the lower surface it is $v_{il0} - v_{il8}$. Because the self-induced normal velocity distributions are the elementary trigonometric functions given in Section C, the linearized integration for the basic mode shapes can be readily completed in closed form.

For a uniform onset flow, the seven basic mode shapes in the slat plane are shown in Figure 8, and their salient characteristics are described below. The distortion of these basic mode shapes by the curvature of the main flow field and by the field of the image slat is treated later in this section.

The singular camber mode B_1 has a constant normal velocity component $v_{il1} = -B_1/2$ which corresponds to a flat plate at an

angle of attack $\Delta_1 \equiv \tan^{-1}(\frac{B_1}{2u_{22}})$ with respect to the flow parallel to the s axis at the velocity u_{22}. The leading edge ordinate for this B_1 mean line is $y_{i6}\big|_{s=-2} = 2B_1/u_{22}$.

The parabolic mean line of the first regular camber mode B_2 has its maximum ordinate $y_{i6}\big|_{s=0} = B_2/u_{22}$ at midchord.

Adding to the offset due to the singular camber mode, the reflexed mean line of the B_3 mode contributes a net leading edge displacement of $y_{i6}\big|_{s=-2} = (\frac{4B_3}{3u_{22}})$ from the real axis in the slat plane. The angular offset Δ_3 of the straight line through the leading and trailing edges of this mean line is $\Delta_3 \equiv \tan^{-1}(\frac{B_3}{3u_{22}})$. This is the angle of zero lift for the strongly reflexed B_3 mode.

The slat's finite leading edge radius ρ is generated by the primary thickness mode B_5.

$$\rho = 8\left(\frac{B_5}{2u_{22}}\right)^2$$

For the B_5 mode, the maximum thickness is at the quarter chord point, and the thickness ratio τ_5 is

$$\tau_5 = \left(\frac{3\sqrt{3}}{4}\right)\left(\frac{B_5}{2u_{22}}\right)$$

In a uniform onset flow, the B_5 mode corresponds to an uncambered Joukowski airfoil which has an airfoil circle offset parameter $\epsilon = B_5/(2u_{22})$. (10, p. 71).

All three of the thickness modes are cusped at the trailing edge, and the regular modes B_6 and B_7 also have cusped leading edges. The B_6 mode has chordwise symmetry about the midchord point, and the thickness ratio τ_6 is

$$\tau_6 = \frac{2B_6}{3u_{22}}$$

The third regular thickness mode B_7 is antisymmetric ahead of and behind the midchord. For $s > 0$, the B_7 mode has "negative thickness."

The main flow velocity components along the slat chord line in the slat plane were derived in Section B. Assuming that the ellipse fineness, the onset flow velocity, and the ellipse angle of attack are initially specified, the normal component v_{i20} and the parallel component u_{i20} of the main flow velocity on the slat chord line are functions of the four slat geometry parameters. As will be discussed in Part III, Section A, the slat chord c_2, the height f_1, and the offset from the origin, f_2, are selected in the half-plane by examination of the distribution of the specified modulating velocity along the real axis which is the transformed ellipse surface. The normal and parallel velocity components then depend only on the fourth parameter, k_6, the slat inclination with respect to the $\mathcal{R}(W)$ axis.

For the typical ellipse test case described in Part III, Section E, the main flow streamline pattern in the half-plane is shown in Figure 4. Within the domain for efficient slats which is to the right of the origin near the real axis, both the convergence and the curvature of the streamlines are slight. If a straight slat chord is placed approximately parallel to one of these main flow streamlines, the streamline curvature will affect the slat loading much more strongly than the streamline convergence will. This is analogous

to the thin airfoil approximation in which the self-induced parallel velocity components along the chord are neglected in the determination of the local airfoil surface slope.

If the slat midchord is aligned with the local main flow in the half-plane, then the parallel component of the main flow, u_{i20}, can be assumed constant along the slat chord. Typically, the variation in the main flow's parallel component is on the order of ten percent of the value of u_{i20} at the slat midchord, and can be neglected. This approximation is consistent with the omission of the self-induced parallel flow components from the linearized slat shape integration. The midchord value $u_{20} \equiv u_{i20}\big|_{s=0}$ is defined as the main flow field's contribution to the constant parallel flow along the slat chord line. Later in this section, the contribution by the image slat field to the total parallel flow, u_{22}, is discussed.

The normal velocity component due to the slight curvature of the main flow streamlines in the slat plane must be taken into account in the slat shape integration. Characteristically, the maximum value of this normal component of the main flow, v_{i20}, is of the same order as the self-induced normal velocity component $v_{i10} \pm v_{i18}$. Including the normal component of the main flow, the local flow shape expression is

$$\left(\frac{dt}{ds}\right)_i = (v_{i10} \pm v_{i18} + v_{i20})/u_{22}$$

To the first order of approximation, the incorporation of v_{i20} into the linearized slat shape integration distorts the slat to

conform to the curvature of the main flow streamlines and thereby removes the effect of this curvature on the slat loading.

The local main flow inclination μ at the slat midchord $W = f_2 + if_1$ in the half-plane is readily obtained from the main flow's parallel and normal components u_{i20} and v_{i20} in the slat plane. The transformation to the slat plane introduces a uniform rotation by the slat angle k_6. Therefore, if the slat angle is initially set equal to zero, then the main flow inclination with respect to the slat at the origin in the S plane is the same as the flow inclination with respect to the real axis in the half-plane. The main flow inclination at the slat midchord is thus given by

$$\mu = \tan^{-1}\left(\frac{-v_{i20}}{u_{i20}}\right)_{s_i=0;k_6=0}$$

The sign convention is chosen so that positive μ corresponds to the normal case of the slat leading edge above and to the left of the midchord point in the half-plane.

After redefining the slat angle as $k_6 \equiv \mu$ to align the midchord with the main flow, the constant parallel component u_{20} is evaluated at the midchord. Because the main flow streamlines are convex toward the real axis in the half-plane, the normal velocity component v_{i20} is negative at the slat leading edge $s = -2$ and increases nearly linearly through the origin (where it is zero by definition) to the trailing edge. This normal component of the main flow field closely resembles the normal velocity distribution induced by a negative

first regular camber mode, $-B_2$. A straight slat chord thus has initial effective camber with respect to the undisturbed main flow field in the half-plane. When the normal component of the main flow is taken into account in the slat shape integration, in the slat plane the slat will appear to be less highly cambered than an airfoil with the same mode coefficients B_I in a uniform onset flow.

The distributions of the normal velocity components along the chord line for the slat $\beta 70$ test case are illustrated in Figure 9. In this case, the first order correction to the slat angle which is described in Section D of Part III has been applied. Because the slat angle was increased beyond the inclination required to align the midchord with the main flow, the v_{i20} distribution is offset toward positive values. Nevertheless, the linear chordwise dependence of v_{i20} as well as the relative magnitudes of the normal velocities induced by the camber and thickness modes are apparent from the illustration.

The velocity field induced on the slat by the distributed singularities on the image slat must also be taken into account in the determination of the slat shape. If the slat in the half-plane is considered as an airfoil in ground effect, a typical slat at a height-to-chord ratio of one half is well within the ground effect range in which the field of the image slat one chord away has significant influence. As is shown in Figure 5, the solution for the image-induced field on the slat is the same as a solution for the slat-induced field on the half-plane if the slat geometry parameters are appropriately redefined. The influence coefficient expressions

derived in Section C (and thus the same section of the digital computer program) can therefore be used to calculate both the slat and the image slat fields.

For the computation of the seven parallel flow influence coefficients u'_{iI} for the image slat field, the redefined slat geometry parameters (f'_1, f'_2, k'_6) given below are used.

$$f'_1 \equiv 2f_1\cos(k_6) = 2f_1k_7 \; ; \quad f'_2 \equiv 2f_1\sin(k_6) = 2f_1k_8$$

$$k'_6 \equiv 2k_6 \; ; \quad k'_7 \equiv \cos(k'_6) \; ; \quad k'_8 \equiv \sin(k'_6)$$

The parallel flow component $B_I u'_{iI}$ evaluated at $h'_i = (c_2/2)\cos(\theta_i)$ on the redefined ground plane then corresponds to the velocity induced at the slat chord station $s_i = 2\cos(\theta_i)$ by the I'th singularity distribution mode on the image slat. The total parallel velocity u_{i8} induced at s_i by the image slat is the sum of the contributions by the seven modes and is negative for all realistic cases.

$$u_{i8} \equiv \sum_{I=1}^{7} B_I u'_{iI}$$

The parallel component of the main flow along the slat chord is approximated by the midchord value u_{20}. It is therefore consistent to consider the parallel component of the image field as constant and equal to the exact image field at the slat midchord.

$$u_8 \equiv u_{i8}\,|_{s_i=0}$$

The total parallel velocity u_{22} along the slat chord is the sum of the main flow and image field contributions.

$$u_{22} = u_8 + u_{20} \; ; \quad u_{22} < u_{20}$$

In the derivation of the equations for the slat-induced velocity which is given on page 25, the expressions for the normal velocity components are shown to be the same as the parallel component equations if the two variables k_7 and k_8 are redefined as follows.

$$k_7'' \equiv \sin(k_6') \qquad k_8'' \equiv -\cos(k_6')$$

The normal component influence coefficients u_{iI}'' for the image slat field are computed from the equations on page 29 using the revised set of slat geometry parameters $(c_2, f_1', f_2', k_6', k_7'', k_8'')$. The total image-induced normal velocity v_{i8} at s_i on the slat is the sum of the products of the seven mode coefficients B_I and the corresponding normal component influence coefficients u_{iI}''.

$$v_{i8} \equiv \sum_{I=1}^{7} B_I u_{iI}''$$

Including the normal flow components induced by the singularities on the slat itself, by the main flow, and by the image slat, the total normal velocity v_{i22} at $s_i = 2\cos(\theta_i)$ on the slat chord is

$$v_{i22} = v_{i8} + v_{i10} \pm v_{i18} + v_{i20}$$

and the constant parallel component is $u_{22} = u_8 + u_{20}$. The slat ordinates in the combined flow field are obtained by integration as on page 40.

Upper Surface

$$y_{i6} = \left(\frac{-2}{u_{22}}\right) \int_0^{\theta_i} \left[v_{i8} + v_{i10} + v_{i18} + v_{i20}\right] \sin(\theta) d\theta$$

Lower Surface

$$y_{i7} = \left(\frac{-2}{u_{22}}\right) \int_0^{\theta_i} \left[v_{i8} + v_{i10} - v_{i18} + v_{i20}\right] \sin(\theta) d\theta$$

The v_{i10} and v_{i18} terms can be readily integrated analytically, and the v_{i8} and v_{i20} terms can be rapidly integrated numerically using a standard Simpson's Rule integration subroutine.

The approximate velocity distribution on the slat in the S plane can be readily obtained. Applying the thin airfoil linearization, the flow speed on the slat surface in the slat plane is the sum of the parallel velocity components evaluated on the slat chord line. The parallel velocity components induced by the distributed singularity modes on the slat are given above in Section C. Antisymmetric above and below the chord line, the parallel velocity q_{i41} contributed by the four camber modes at the chord station $s_i = 2\cos\theta_i$ is, on the upper surface,

$$q_{i41} = (B_1/2)\tan(\theta_i/2) + B_2 \sin\theta_i - B_3 \sin 2\theta_i + B_4 \sin 3\theta_i$$

The sum of the constant parallel component of the main flow, u_{22}, and the contributions of the three thickness modes is defined as q_{i40} and is symmetric above and below the chord line.

$$q_{i40} = u_{22} + (B_5/2)(1 - 2\cos\theta_i) - B_6 \cos 2\theta_i + B_7 \cos 3\theta_i$$

Along the upper slat surface, the linearized flow speed q_{il6} is

$$q_{il6} = q_{i40} + q_{i41}$$

and the speed q_{il7} on the slat lower surface is

$$q_{il7} = q_{i40} - q_{i41}$$

Near the leading edge, this linearized approximation to the flow speed on the slat surface is not valid. As the argument θ approaches the leading edge value π, both the parallel velocity component $u_{ill} = (B_1/2)\tan(\theta_i/2)$ induced by the singular camber mode B_1 and the normal velocity component $v_{il5} = (B_5/2)[\tan(\theta_i/2) - 2\sin\theta_i]$ induced by the primary thickness mode B_5 are unbounded.

A higher order approximation for the slat nose flow can be obtained by Allen's technique (13). To replace the two singular terms, the flow solution for the uncambered Joukowski airfoil corresponding to the B_5 thickness mode at the angle of attack Δ_1

$$\Delta_1 = \tan^{-1}\left(\frac{B_1}{2u_{22}}\right) \simeq \left(\frac{B_1}{2u_{22}}\right)$$

appropriate to the flat plate camber mode B_1 is used. This basic nose flow velocity q_{iN} is given by Riegels (14) as

$$q_{iN} = u_{22}\left\{\frac{\cos\Delta_1[(1+\epsilon)\sin\theta_i - \epsilon\sin2\theta_i] + \sin\Delta_1(1-\cos\theta_i)(1-2\epsilon\cos\theta_i)}{[\sin^2\theta_i + \epsilon^2(\cos\theta_i - \cos2\theta_i)^2]^{\frac{1}{2}}}\right\}$$

$$\epsilon \equiv \left(\frac{B_5}{2u_{22}}\right)$$

Because the five remaining modes are regular at the slat leading edge, the parallel components of their induced velocity fields on the chord line can be included as perturbations to this basic nose flow solution. The total velocity q_{il6} on the upper surface of the slat nose in the slat plane is then given by

$$q_{il6} = q_{iN} + B_2 \sin\theta_i - B_3 \sin 2\theta_i + B_4 \sin 3\theta_i - B_6 \cos 2\theta_i + B_7 \cos 3\theta_i$$

The excellent inherent accuracy of this technique for obtaining a higher order approximation to the nose flow on an airfoil in a uniform onset flow is thoroughly discussed by Allen. As discussed earlier in this section, additional approximations for the non-uniform main flow and image slat field are introduced into this semi-inverse solution to linearize the slat shape integration. To a first order of approximation, the influence of the onset flow curvature on the slat loading was removed by including the normal components of the main and image flow fields in the expression for the local slat surface slope. However, higher order effects of the flow curvature and the influence of the small variations of the parallel flow component from the midchord value u_{22} have not been taken into account.

G. Mappings from Slat Plane to Ellipse Plane

The slat ordinates (s; $t = y_6$, y_7) obtained by integration in the slat plane can be mapped to the ellipse plane using the following transformation sequence. The mapping from the slat plane $S = s+it$ to the half-plane $W = x_3 + iy_3$ is

$$W = \left(\frac{c_2}{4}\right) S\, e^{-ik_6} + f_2 + if_1$$

and can be expressed as

$$x_3 = (\frac{c_2}{4})\ (k_7 s + k_8 t) + f_2 \qquad y_3 = (\frac{c_2}{4})\ (k_7 t - k_8 s) + f_1$$

The mapping derivative $|dS/dW| = 4/c_2$ is defined as M_3.

From the half-plane to the circle plane $z = x_2 + iy_2$, the mapping is

$$z = c_3\ (\frac{W+i}{W-i})$$

This transformation can be written in the form

$$x_2 = \frac{c_3(x_3^2 + y_3^2 - 1)}{x_3^2 + y_3^3 - 2y_3 + 1} \qquad y_2 = \frac{2c_3 x_3}{x_3^2 + y_3^2 - 2y_3 + 1}$$

The corresponding mapping derivative $M_2 \equiv |dz/dW|$ is given by

$$M_2 = \frac{2c_3}{|W^2 - 2iW - 1|}$$

$$M_2 = \frac{2c_3}{[(x_3^2 - y_3^2 + 2y_3 - 1)^2 + 4x_3^2(y_3 - 1)^2]^{\frac{1}{2}}}$$

Finally, the Joukowski transformation to the ellipse plane $Z = x_1 + iy_1$ is

$$Z = z + \frac{c_7}{4z}$$

$$x_1 = x_2 \left[1 + \frac{c_7}{4(x_2^2 + y_2^2)}\right] \qquad y_1 = y_2 \left[1 - \frac{c_7}{4(x_2^2 + y_2^2)}\right]$$

The mapping derivative $|dZ/dz|$ is designated M_1

$$M_1 = \left| 1 - \frac{c_7}{4z^2} \right|$$

$$M_1 = \frac{\left\{ \left[1 - c_7(x_2^2 - y_2^2) \right]^2 + (2c_7 x_2 y_2)^2 \right\}^{\frac{1}{2}}}{4\left[(x_2^2 - y_2^2)^2 + (2x_2 y_2)^2 \right]}$$

In terms of the three mapping derivatives and a flow speed q_{il4} in the slat plane, the flow speed q_{il1} at the corresponding point in the ellipse plane is

$$q_{il1} = \left(\frac{M_3}{M_1 M_2} \right) q_{il4}$$

For an onset flow velocity, U, of unity in the ellipse plane, the pressure coefficient C_{p_i} defined as

$$C_{p_i} \equiv \frac{P - P_\infty}{(\rho/2)U^2}$$

is given by

$$C_{p_i} = 1 - q_{il1}^2$$

III. THE SEMI-INVERSE SLAT DESIGN TECHNIQUE

A. Selection of Slat Location in Half-Plane

Using the analysis presented in Part II, a digital computer program can be written which will rapidly generate a slat which induces a velocity field that closely matches the specified modulating velocity distribution on the ellipse. Trial solutions utilizing this semi-inverse slat design technique were conducted on the California Institute of Technology's time-sharing computer system. As described below, the selection of the slat location introduces an element of judgement into the solution, and therefore the direct operator interaction with the solution which the time-sharing system affords was very useful. For the test cases, the desired pressure distribution was specified directly on the ellipse because, as discussed in Part I, the specified flow on an arbitrary airfoil can be mapped through the circle plane to the ellipse plane. The ellipse thickness ratio and angle of attack were selected to provide a realistic model of the flow environment in which a slat for a thin airfoil must operate. A description of the technique used for the trial semi-inverse solutions follows.

The initial step in the solution was the calculation of the modulating velocity w_{i2} which the slat must induce at the matching station h_i on the real axis in the half-plane. The critical high velocity region on the upper nose surface of the ellipse corresponds to the segment of the $R(W)$ axis just to the right of the origin, and therefore closely-spaced matching stations were designated in this region. Using the successive transformations from the half-plane to the

ellipse plane which are given in Part II, Section G, the ellipse station (x_{il}, y_{il}) corresponding to each h_i was determined. The pressure coefficient C_{p_i} at each of these stations was obtained from a graph of the specified pressure distribution on the ellipse. For an onset flow velocity of unity, the specified velocity q_{il8} on the ellipse is

$$q_{il8} = (1-C_{p_i})^{\frac{1}{2}}$$

Employing the mapping derivatives $M_2 = |dz/dW|$ and $M_1 \equiv |dZ/dz|$, the specified velocity in the half-plane is defined as $w_{i4} \equiv M_1 M_2 q_{il8}$. The main flow velocity at h_i on the $\mathcal{R}(W)$ axis is designated w_{i3}, and the specified modulating velocity w_{i2} is then given by $w_{i2} = w_{i4} - w_{i3}$.

Selection of the slat location in the half-plane is the next major step of the semi-inverse solution. A fundamental characteristic of this slat design technique is that the fine modulation of the slat-induced velocity field is accomplished by adjusting the singularity distribution on the fixed slat chord line rather than by altering the position of a slat of fixed camber and thickness. An approximate specification of the slat location is therefore adequate, because the least squares solution for the seven singularity distribution mode coefficients B_I performs the fine matching to the specified modulating velocity distribution. For a set of slat locations within a local region of the half-plane, this semi-inverse solution will generate a class of slats of varying shape, all of which have induced velocity fields that closely match the desired induced field.

The insight required for the proper initial selection of the slat location parameters (f_1, f_2) and the slat chord c_2 is obtained by comparison of the graph of the distribution of the specified modulating velocity along the $R(W)$ axis with the characteristic influence coefficient curves shown in Figure 6.

For typically small slat inclinations, the peak induced velocities for the singular B_1 and reflexed B_3 camber modes occur under the slat quarter chord, and the flow induced by the regular B_2 camber mode reaches a maximum under the slat midchord. Therefore, the slat offset from the origin, f_2, is selected to place the peak of the specified modulating velocity curve between the slat mid- and quarter-chord points. The appropriate slat chord and height f_1 are estimated from the width, the height-to-width ratio, and the tailoff slope of the specified modulating velocity curve.

The small matrix inversion required by the least squares matching can be completed extremely rapidly by the digital computer. The mode coefficients B_I selected by an initial solution can therefore be used as qualitative indicators for the selection of improved slat geometry parameters (c_2, f_1, f_2). For example, the loading of the slat trailing edge which is indicated by a negative reflex camber coefficient B_3 suggests that the slat offset f_2 should be increased. A relatively large third regular camber mode coefficient B_4 loads both ends of the slat, thus broadening the induced field, and indicates that the initial slat chord c_2 was too small. After a series of trial solutions to gain experience with the technique, the appropriate alterations of the slat geometry parameters become quite evident.

The loading distribution on the slat can be favorably influenced by the proper choice of slat location. The singular camber mode B_1 contributes a sharp pressure peak at the slat leading edge which may induce boundary layer separation on the slat. If an initial inversion solution yields $B_1 > B_2$, a decrease in slat offset f_2 is indicated. A second inversion solution will then favor the distributed loading of the first regular camber mode B_2, which is symmetric about the slat midchord.

B. Positive Slat Thickness Constraint

In the least squares solution described in Part II, Section D, no sign constraint was placed upon the camber and thickness mode coefficients B_I. As is apparent from the graphs of the influence coefficients (Figure 6), positive values of the primary and first regular thickness mode coefficients, B_5 and B_6, induce positive velocities on the half-plane surface under the slat. Slat thickness thus increases the velocity past the ellipse nose. Because the purpose of the slat is to decrease the nose velocity by contributing a strong negative flow component, this detrimental effect of slat thickness must be counteracted by increased backflow induced by additional positive camber on the slat. From the design standpoint, therefore, slat thickness should be reduced as far as is permitted by considerations of slat structural strength and of slat nose C_p which becomes increasingly negative with decreasing slat nose radius.

During some initial solutions for the slat shape mode coefficients, negative values for the B_5 and B_6 thickness mode coefficients

were obtained. For these cases, to match the particular specified modulating velocity distribution, the unconstrained inversion solution employed the backflow field induced by negative thickness terms as well as the negative velocity field induced by the positive camber modes. The computer program was therefore modified to constrain the slat shape solutions to physically realizable positive thickness cases.

The program was rewritten to allow completion of the matrix inversion in the least squares solution using either the full seven by seven influence coefficient product matrix A or a four by four matrix containing only the terms corresponding to the four camber modes. This modification provided the alternative of a restricted matching solution employing only the one singular and three regular camber distributions.

If the initial unconstrained inversion solution for the seven mode coefficients yielded a negative value for the primary thickness mode coefficient B_5, a constrained solution was then performed. First, the program demanded that the minimum acceptable slat thickness distribution be specified in terms of the three thickness mode coefficients. The induced velocity field corresponding to this specified slat thickness distribution was then calculated. Next, a restricted slat inversion solution was conducted to select the four camber coefficients required for cancelling this thickness-induced field in addition to matching the specified modulating velocity distribution.

For these cases requiring constrained solutions, the minimum acceptable slat thickness distribution is specified as a superposition of the B_5, B_6, and B_7 thickness modes. As discussed in Part II, Section F, the slat thickness in the slat plane is a linear function of the mode coefficients and the parallel velocity component u_{22} along the chord line. For the primary thickness mode alone, the maximum thickness to chord ratio for the slat is

$$\tau_5 = .65\, B_5/u_{22}$$

Using the fifth mode influence coefficients u_{i5} and the slat plane to half-plane mapping derivative $4/c_2$, the offset velocity w_{i5} corresponding to this prescribed slat thickness can be calculated at each matching station

$$w_{i5} = (8/c_2)B_5u_{i5} = (8/c_2)\ 1.54\ \tau_5u_{22}u_{i5}$$

The specified modulating velocity w_{i2} is defined as the difference between the specified velocity w_{i4} and the main flow velocity w_{i3} at h_i in the half-plane

$$w_{i2} \equiv w_{i4} - w_{i3}$$

The biased specified modulating velocity w'_{i2} is defined as the specified modulating velocity minus the offset velocity induced by the prescribed slat thickness distribution.

$$w'_{i2} \equiv w_{i4} - w_{i3} - w_{i5}$$

A restricted inversion solution for the four camber mode coefficients required to match this biased specified modulating velocity distribution can be conducted. The total slat-induced velocity w_{i1} corresponding to these camber mode coefficients plus the prescribed thickness mode coefficients will then match the specified modulating velocity w_{i2}. For the slat β70 test case, the half-plane velocities w_{i1}, w_{i2}, and the biased w'_{i2} are shown in Figure 10.

C. Iteration Loop Required to Maintain Kutta Condition on Ellipse

Because of the small increment of compensating vorticity Γ_c which is required to maintain the Kutta condition on the ellipse when a slat is added, an iteration on the least squares solution is necessary to achieve an accurate matching to the specified velocity distribution on the ellipse. Initially, the velocity distribution on the unslatted ellipse is calculated by assuming that the total ellipse circulation Γ_t is the basic vorticity Γ_0 required to null the crossflow at the trailing edge. For the first least squares solution, the specified modulating velocity w_{i2} is defined as the difference between the specified velocity w_{i4} and the initial value of the main flow velocity w_{i3} corresponding to the circulation $\Gamma_t = \Gamma_0$. However, the addition of the slat vorticity Γ_s required to match this specified modulating velocity distribution increases the total ellipse circulation to $\Gamma_t = \Gamma_0 + \Gamma_c$. As a result, the final velocity on the ellipse nose will be somewhat higher than the specified velocity.

A revised distribution of specified modulating velocity $w''_{i2} \equiv w_{i2} + \Delta w_{i2}$ is then obtained using a revised value of the main flow

velocity $w'_{i4} \equiv w_{i4} + \Delta w_{i4}$ corresponding to the increased total ellipse circulation. The slight increase in slat circulation $\Gamma'_s \equiv \Gamma_s + \Delta\Gamma_s$ that is required to match the increase in the specified modulating field will in turn necessitate an additional increment of compensating vorticity, $\Delta\Gamma_c$, thus further increasing the total circulation to Γ'_t.

$$\Gamma'_t \equiv \Gamma_0 + \Gamma_c + \Delta\Gamma_c$$

This iteration can be continued until the additional increments of circulation are insignificant with respect to the other approximations in the solution.

For realistic slat cases, the initial compensating vorticity increment Γ_c is not more than a few percent of the basic ellipse circulation Γ_0, and the iteration converges extremely rapidly. The compensating vorticity for the typical slat β70 test case is only six tenths of a percent of the basic circulation.

D. First Order Correction to Slat Inclination

During the initial semi-inverse solutions, it was observed that the slat shapes generated by the linearized integration were offset significantly from the assumed position of the singularity distribution along the real axis in the slat plane. This offset was primarily due to the relatively large component of the reflex camber mode B_3 selected by the least squares matching in order to concentrate the slat vorticity near the quarter chord. Referring to page 41, the angular offset contributed by the reflex camber mode is designated

Δ_3 and is the angle of zero lift for this mode. The singular or flat plate camber mode B_1 also contributes an increment Δ_1 to the net angular offset of the slat mean line.

A first order correction for this angular offset can be readily incorporated in the solution. An initial least squares inversion is conducted with the slat angle k_6 conventionally defined to align the slat midchord parallel to the main flow. Using the mode coefficients B_1 and B_3 from this initial inversion, the two angular offsets Δ_1 and Δ_3 can be calculated. The slat angle is then redefined as the original slat inclination plus the two offsets.

$$k'_6 \equiv k_6 + \Delta_1 + \Delta_3$$

A second least squares matching is conducted using the redefined slat angle k'_6. The increase in slat inclination slightly displaces the singularities on the forward half of the slat away from the matching stations on the real axis of the half-plane. Therefore, the second inversion solution will select slightly higher camber mode coefficients to match the specified modulating velocity. As a result, a small residual offset of the slat mean line will remain after the first order correction. Higher order corrections to reduce the offset between the assumed position of the singularities and the geometric mean line of the generated slat to less than half the slat thickness would be inconsistent with the basic thin airfoil approximations in the slat analysis.

E. Slat Design Example: Slat β70

As a difficult test case for this semi-inverse slat design technique, an ellipse with a nose radius of one percent of chord, a typical R_0 for a high-speed airfoil, was chosen. A lift coefficient of 2.12 at an angle-of-attack of .3 radians or 17.2° was selected as representative. Without a leading edge slat, this 14.1% thick ellipse would, in theory, develop an absurd nose pressure coefficient $C_{p_{nose}} = -21.8$.

The specified pressure distribution for the slat β70 test case is shown in Figure 11. This distribution incorporates the general characteristics of a desirable nose pressure gradient but is not intended to represent a separation-free distribution for a particular full-scale airfoil. A minimum pressure coefficient of approximately minus nine was selected as a realistic limit for low-speed operation of a thin airfoil at a moderate lift coefficient. Because the boundary layer at the nose is typically laminar, a mild pressure gradient similar to the moderate initial slope of this specified distribution is required to avoid development of a separation bubble. Behind the suction peak, the steady decrease of the adverse pressure gradient as exhibited by this specified distribution is a necessary condition for maintaining unseparated laminar flow. Beyond the predicted transition point for a particular airfoil, a considerably more severe adverse pressure gradient could be specified.

For the slat β70 design example, a constrained semi-inverse solution was required. A representative minimum acceptable thickness distribution was specified, and a restricted inversion

solution for the camber mode coefficients was then conducted. The prescribed value of the primary thickness mode coefficient corresponded to a slat thickness ratio $\tau_5 = .1$ in the slat plane. In addition, to increase the slat thickness between the midchord and the trailing edge, a negative B_7 thickness mode coefficient equal in magnitude to twenty percent of the B_5 mode coefficient was also specified.

The pressure distribution calculated by this semi-inverse solution for the nose of the ellipse with slat β70 is shown in Figure 11. The location of the matching stations along the ellipse chord, the specified pressure coefficients at these stations, and the pressure coefficients achieved with the semi-inverse solution are given in the Appendix. The very close agreement between the specified and solution pressure distributions is typical of the accurate matching which can be achieved with this semi-inverse design technique once an appropriate slat chord location in the half-plane has been selected. Although the pressure distribution over the first five percent of the ellipse chord is drastically altered by the addition of slat β70, the forward stagnation point is shifted only half a percent of chord from its original position near the nine percent chord station on the lower surface of the ellipse.

The distributions of the specified modulating velocity w_{i2} and the biased specified modulating velocity w'_{i2} in the half-plane are shown in Figure 10. For the prescribed slat thickness distribution, the maximum offset between w_{i2} and w'_{i2} is approximately twenty percent. Even for this very thin slat, the adverse velocity

field induced by the slat thickness is significant. The distribution of slat-induced velocity w_{il} which was achieved with the semi-inverse solution for slat β70 is also plotted in Figure 10.

In the slat plane, slat β70 has the shape shown in Figure 12. Because of the slight curvature of the main flow in the S plane, the effective camber of the slat is somewhat greater than is apparent from this illustration. In this plane, the large reflex component of the slat camber distribution is evident. After the first order correction to the slat inclination, the maximum residual offset between the geometric mean line of the slat and the line of singularities on the $\mathcal{R}(S)$ axis is approximately equal to the slat thickness.

The ellipse plane configuration for slat β70 is illustrated in Figure 13. Measured in percent of the ellipse chord, the ellipse nose radius is one percent, the slat standoff from the nose is approximately two percent and the slat chord is five percent. As shown in Figure 11, this small slat close to the ellipse nose is very effective in reducing the extreme nose suction peak of the unslatted ellipse.

For the slat itself, the pressure distribution computed by the approximate method outlined in Section F of the Analysis is plotted in Figure 14. A suction peak of minus fifteen is predicted immediately behind the slat nose, and the pressure coefficient is more negative than the ellipse nose limit of minus nine over the forward half of the slat. The loop in the upper and lower surface pressure coefficient curves near the trailing edge is a result of the strong reflex component of the slat camber distribution. Because

of the cusped trailing edge, the slat lacks a rear stagnation point.

For a specific full-scale design case, a slat boundary-layer analysis following the semi-inverse solution is required to determine whether the slat pressure distribution is acceptable. If necessary, the slat loading can be altered by selecting modified slat geometry parameters as discussed in Section A of this part. In addition, for restricted semi-inverse solutions, the prescribed thickness distribution on the slat can be modified to improve the pressure distribution.

F. Comparison with Douglas-Neumann Direct Solution.

For the slat β70 configuration, the flow solution calculated by this semi-inverse technique was compared with the Douglas-Neumann direct potential flow solution (5).

On the ellipse nose, the agreement between the direct and semi-inverse solutions is good. As illustrated in Figure 11, the maximum difference between the two solutions is approximately four percent.

However, on the slat the pressure coefficients predicted by the direct and semi-inverse solutions diverge somewhat at both the leading and trailing edges. Near the slat nose, the smoother pressure distribution from the Douglas-Neumann solution can be assumed to be the most accurate. A higher order approximate solution for the slat nose in a non-uniform onset flow is apparently required. At the slat trailing edge, the pressure distribution predicted by the semi-inverse solution is more accurate because the Douglas-Neumann solution is inherently unable to treat the cusped

slat trailing edge exactly. The scatter in the direct solution C_p values near the trailing edge is a characteristic result of attempts to treat the cusped trailing edge case with the Douglas-Neumann program.

IV. CONCLUSIONS

The semi-inverse design technique described in this thesis will generate a leading edge slat which will induce the modulating field required to match a specified pressure distribution on the nose of an ellipse. The digital computer program for the semi-inverse solution is straightforward and can be executed rapidly. After a few initial semi-inverse solutions for a particular design case, the most appropriate choice of slat chord location in the half-plane is apparent. The ellipse nose flow calculated by the semi-inverse solution agrees well with the flow predicted by the Douglas-Neumann direct solution for the slat geometry generated by the semi-inverse technique.

Several significant qualitative insights into the slat design problem were obtained from the solutions conducted using this semi-inverse technique. On a thin airfoil with a severe suction peak at the nose, a small, highly cambered slat close to the leading edge is desirable. For an efficient slat design, the slat vorticity should be concentrated near the region of the airfoil nose which requires the highest modulating backflow. Because the main flow streamlines near the nose of a heavily loaded airfoil are strongly curved, an efficient slat which will lie approximately along one of these zero order streamlines will be very highly cambered. Even for thin slats, at efficient standoff-to-chord ratios the adverse velocity field induced by the slat thickness components is of the same order as the backflow field induced by the camber components and must be

compensated for by additional slat vorticity. At a typical slat standoff ratio of one-half, the flow on the airfoil nose is quite sensitive to the details of the distribution of camber and thickness along the slat chord line.

From the insight provided by the semi-inverse solutions, it is apparent that the alternate trial-and-error approach to slat design by a sequence of direct solutions is unattractive. The sensitivity of the airfoil nose flow to the slat camber and thickness distributions precludes experimental "optimization" of a slat design. A prohibitively large number of models would be required to adequately cover the full range of slat shape parameters. Similarly, a very extensive series of direct numerical solutions would be necessary to determine by trial and error the slat shape and position required to induce a specified modulating field.

The basic semi-inverse solution of this thesis can be extended into a slat design technique applicable to a general airfoil. The appropriate numerical technique for mapping an arbitrary airfoil to the circle plane must be incorporated into the slat design program. In addition, approximate laminar and turbulent boundary-layer calculations can be included to compute the specified pressure distribution on the airfoil nose. After the semi-inverse solution has generated a slat, the boundary-layer analysis subroutine can be used to determine whether the slat boundary layer can tolerate the imposed pressure distribution. A higher order approximate

solution for the slat nose flow will be required for accurate prediction of the slat boundary-layer behavior. By extending the basic semi-inverse solution in this manner, a semi-inverse solution which is directly applicable to practical slat design problems can be obtained.

REFERENCES

1. Pleines, W., "Application of the Slotted Wing to Steep Gradient and STOL Aircraft," in Lachmann, G. V., ed., Boundary Layer and Flow Control, Vol. I. Pergamon Press, London, 1961.

2. Weick, F. E. and Sanders, R., "Wind Tunnel Tests on Combinations of a Wing with Fixed Auxiliary Airfoils Having Various Chords and Profiles," NACA Report No. 472, 1933.

3. Quinn, J. H., Jr., "Tests of the NACA 64_1A212 Airfoil Section with a Slat, a Double-Slotted Flap, and Boundary Layer Control by Suction," NACA TN 1293, 1947.

4. Lindfield, A. W., "Brief Review of Theoretical Interpretations of the Slot Effect," in Lachmann, G. V., ed., Boundary Layer and Flow Control, Vol. I, Pergamon Press, London, 1961.

5. Hess, J. L. and Smith, A. M. O., "Calculation of Potential Flow About Arbitrary Bodies," in Progress in Aeronautical Sciences, Vol. 8. Pergamon Press, New York, 1966.

6. Glauert, H., The Elements of Aerofoil and Airscrew Theory, Macmillan Co., New York, 1944.

7. Thwaites, Brian, ed., Incompressible Aerodynamics, Clarendon Press, 1960.

8. Cooke, J. C., and Brebner, G. C., "The Nature of Separation and its Prevention by Geometric Design in a

Wholly Subsonic Flow," in Lachmann, G. V., ed., Boundary Layer and Flow Control, Vol. I, Pergamon Press, London, 1961.

9. Schlichting, H., Boundary Layer Theory, 6th ed., McGraw-Hill, New York, 1968.

10. Jones, R. T., and Cohen, D., "Aerodynamics of Wings at High Speeds," in Donovan, A. F. and Lawrence, H. R., ed., Aerodynamic Components of Aircraft at High Speeds, High Speed Aerodynamics and Jet Propulsion, Vol. 7, Princeton University Press, Princeton, N. J., 1957, p. 15.

11. Franklin, J. N., Matrix Theory, Prentice-Hall, Englewood Cliffs, N. J., 1968, p. 50.

12. Kármán, T. v., and Burgers, J. M., "General Aerodynamic Theory - Perfect Fluids," in Durand, W. F., ed., Aerodynamic Theory, Vol. II, Dover, New York, 1963, p. 71.

13. Allen, H. J., "General Theory of Airfoil Sections Having Arbitrary Shape or Pressure Distribution," NACA Report 833, 1945.

14. Riegels, F. W., Aerofoil Sections, Butterworths, London, 1961, p. 68.

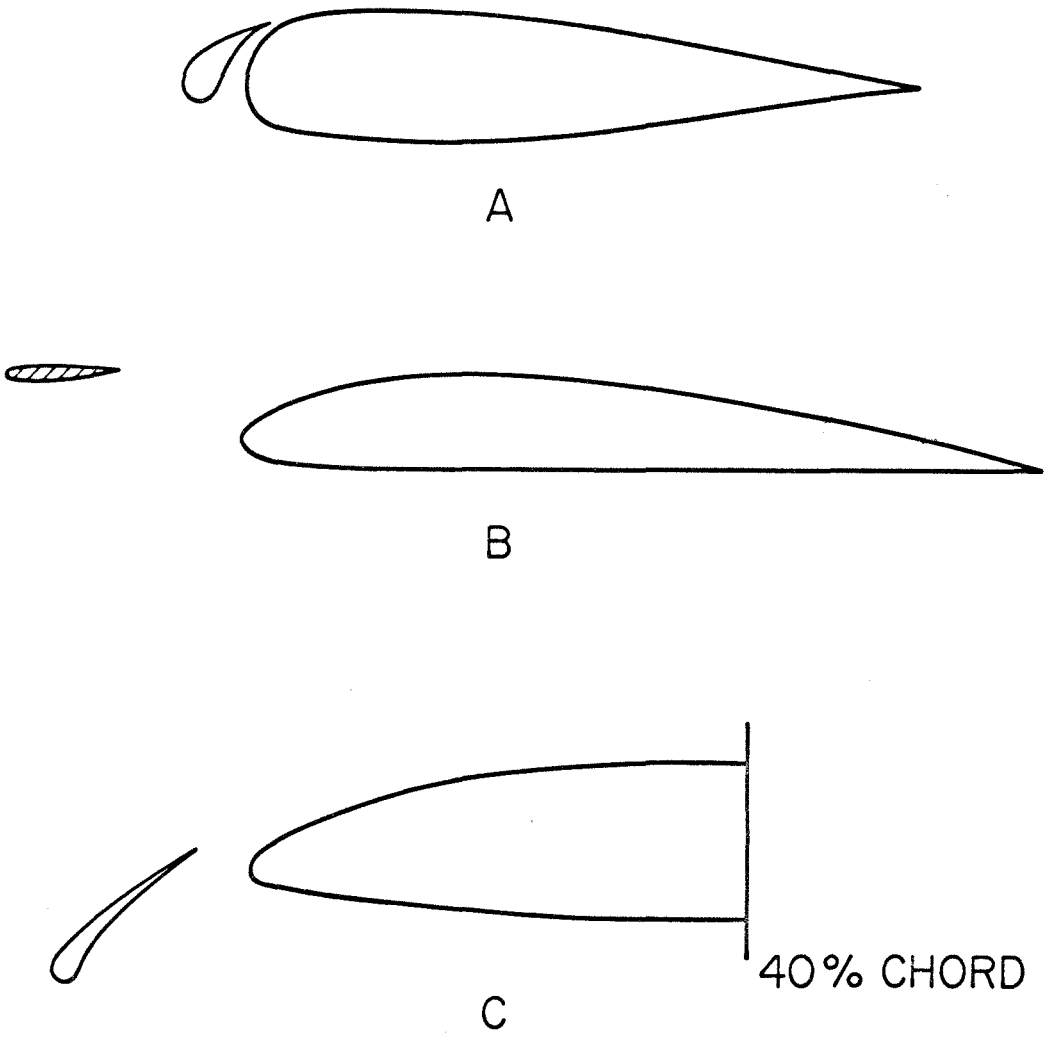

Figure 1. Slat Configurations

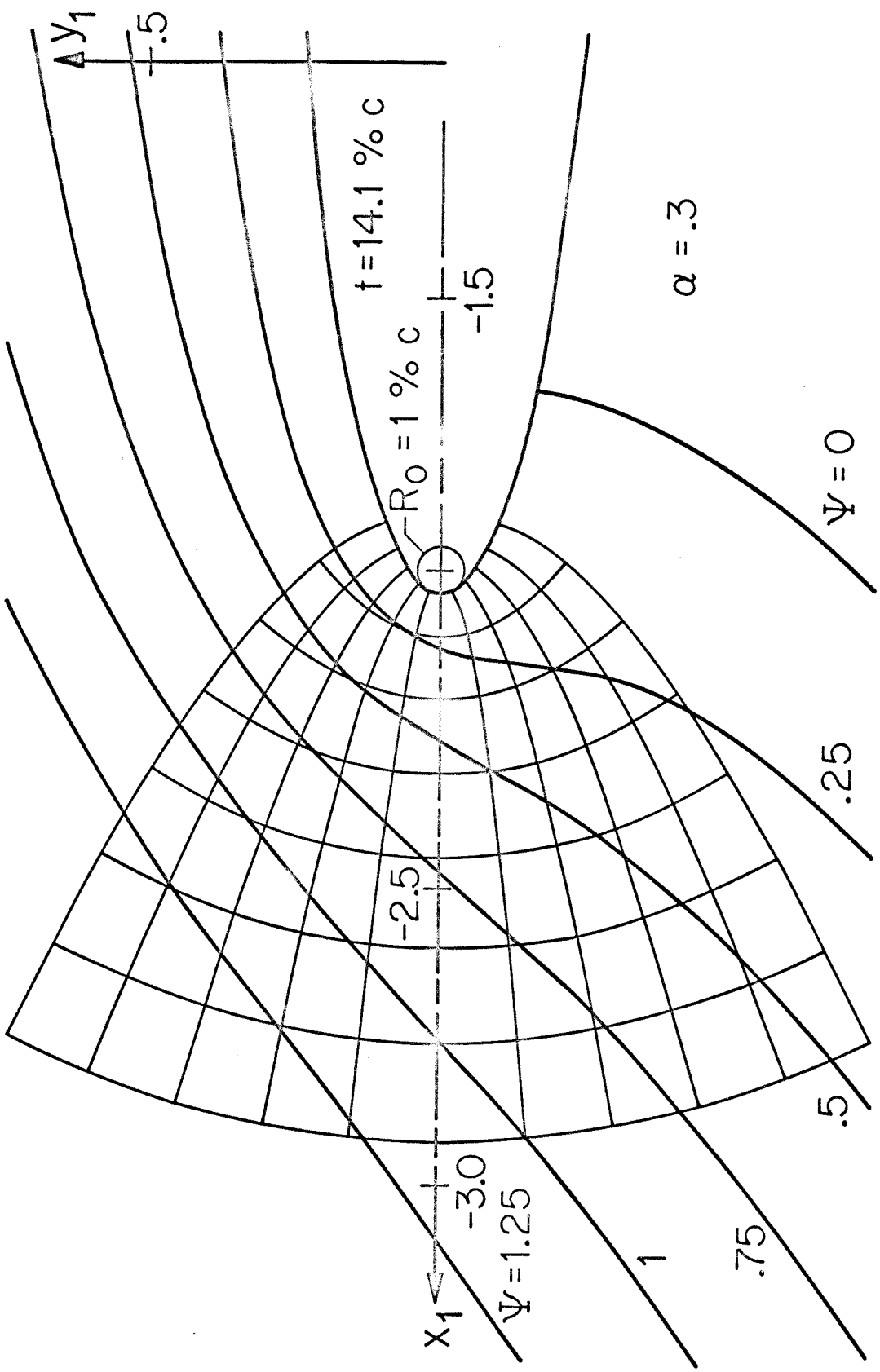

Figure 2. Ellipse Plane Nose Flow

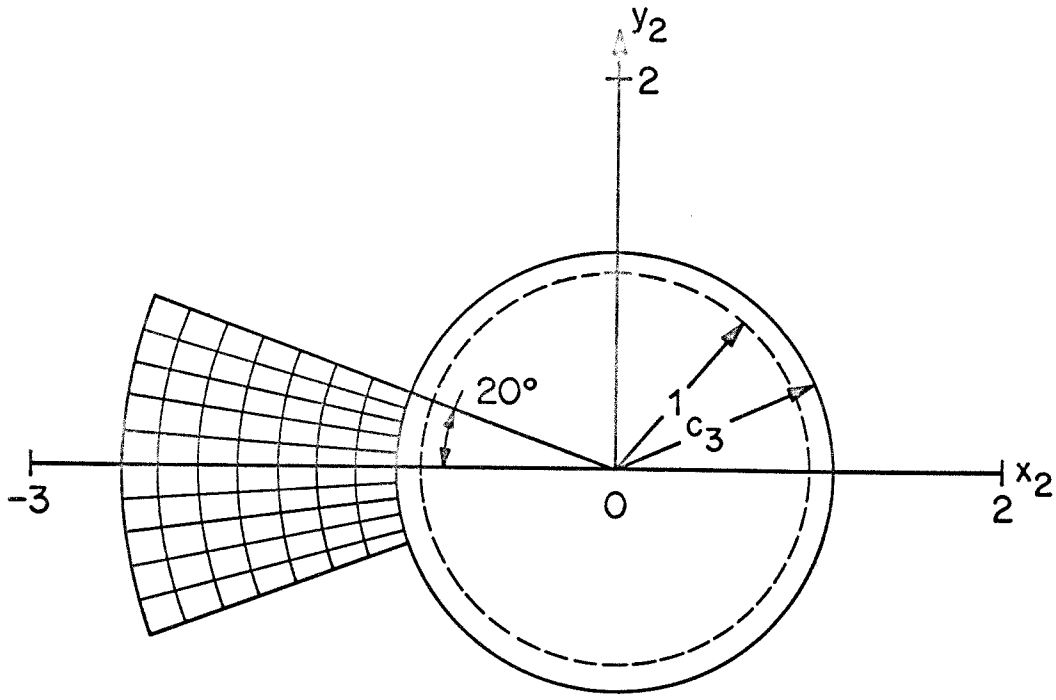

$c_3 = 1.141$ FOR $\tau_{ELLIPSE} = .14$

$z = x_2 + iy_2$

Figure 3. Circle Plane

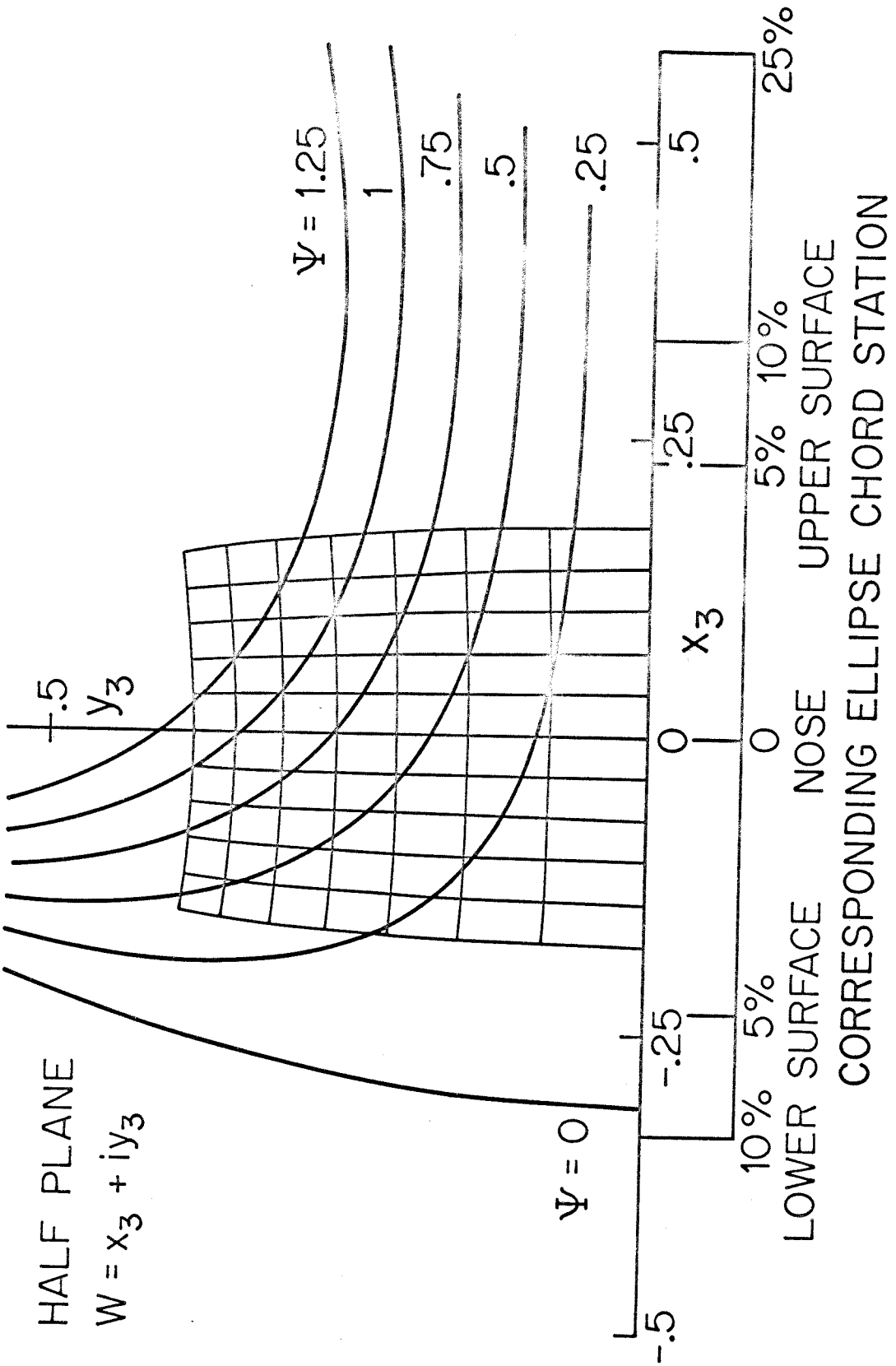

Figure 4. Main Flow in Half-Plane

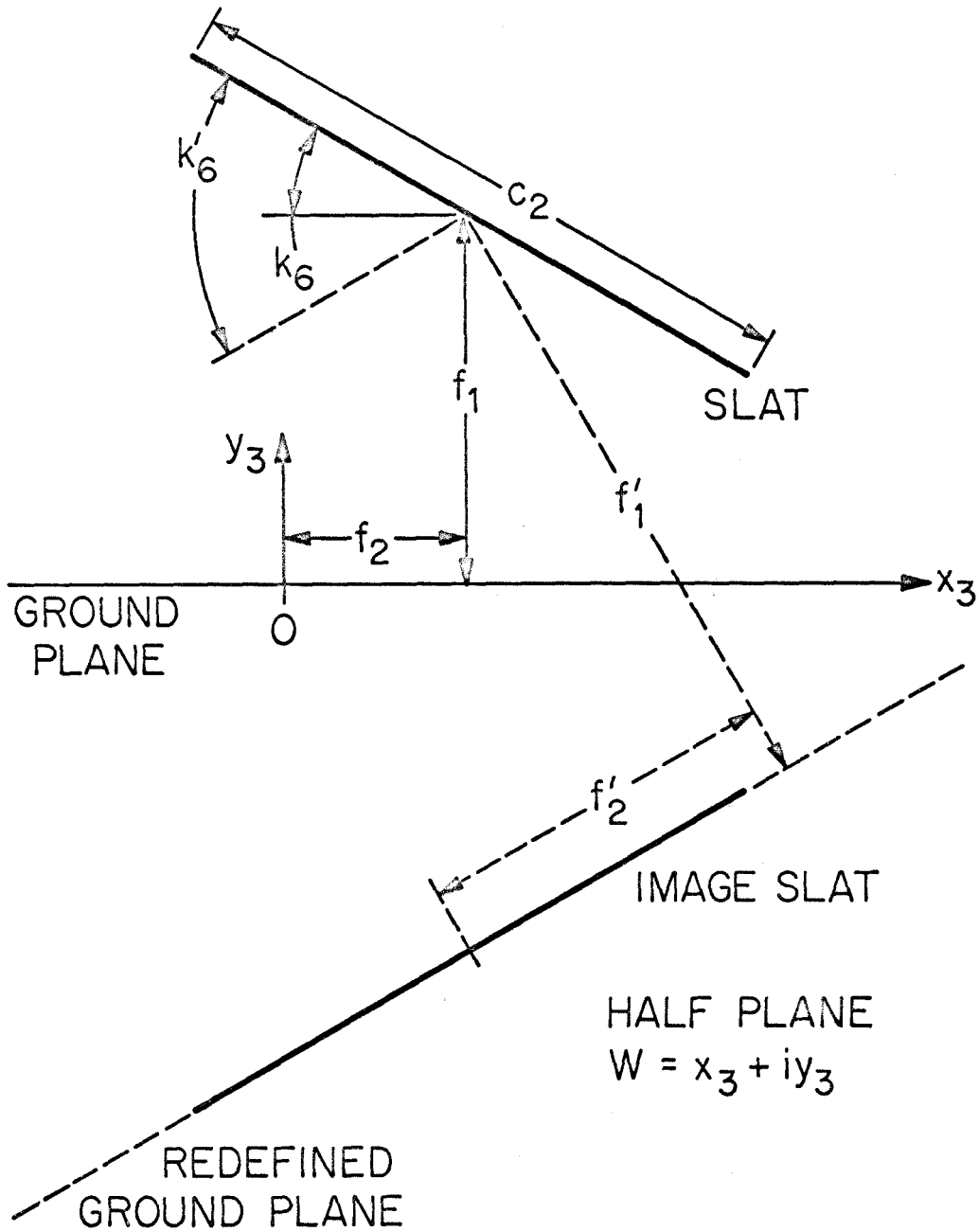

Figure 5. Slat and Image Slat Geometry

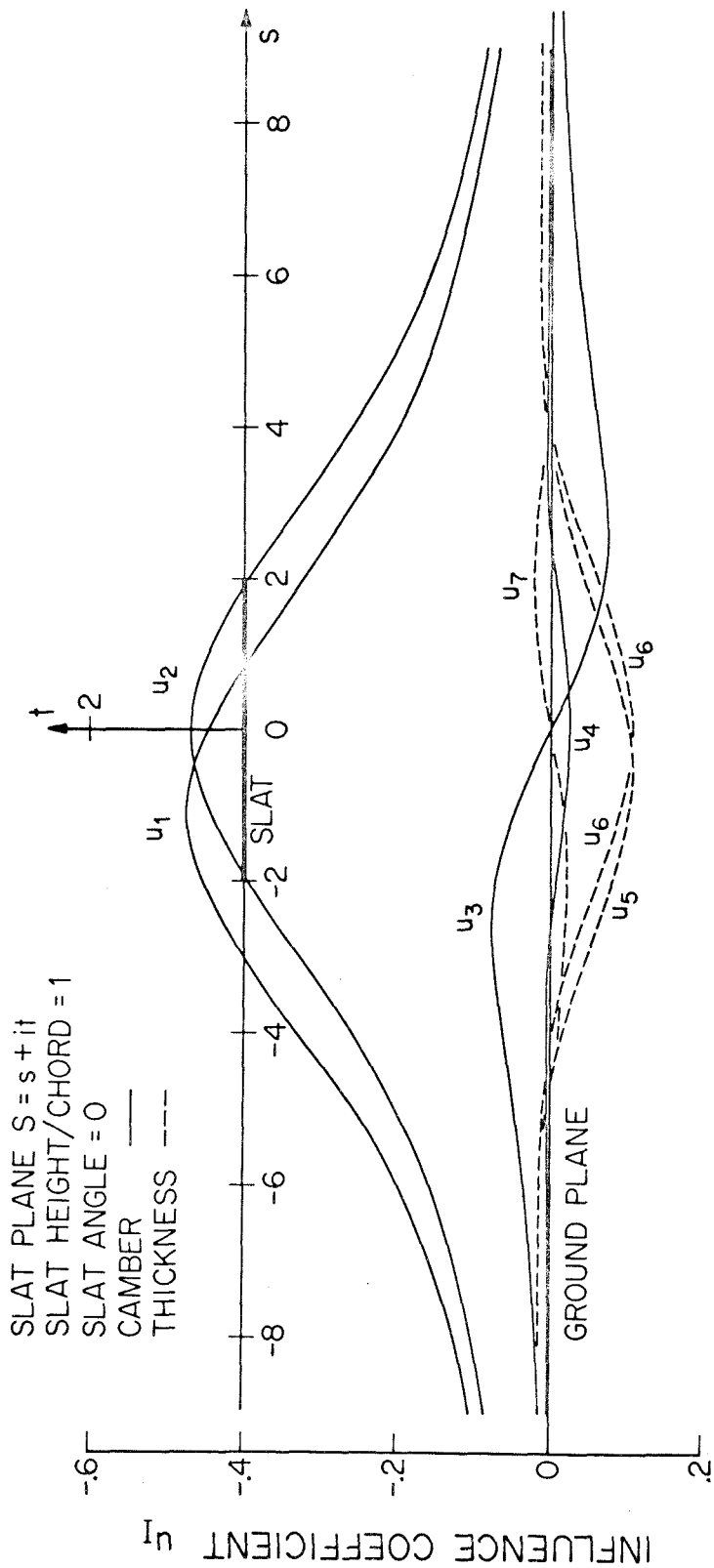

Figure 6A. Influence Coefficients

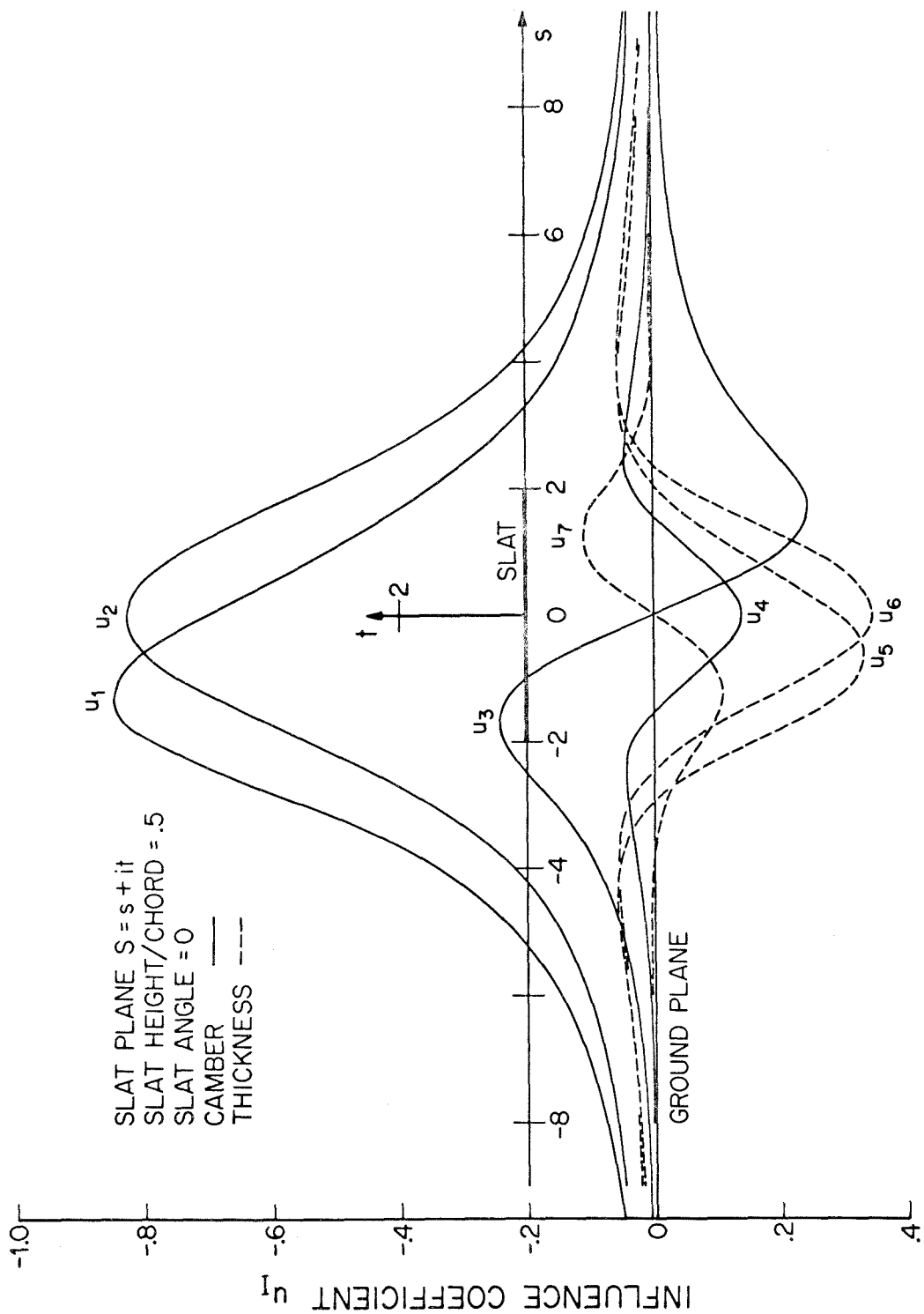

Figure 6B. Influence Coefficients

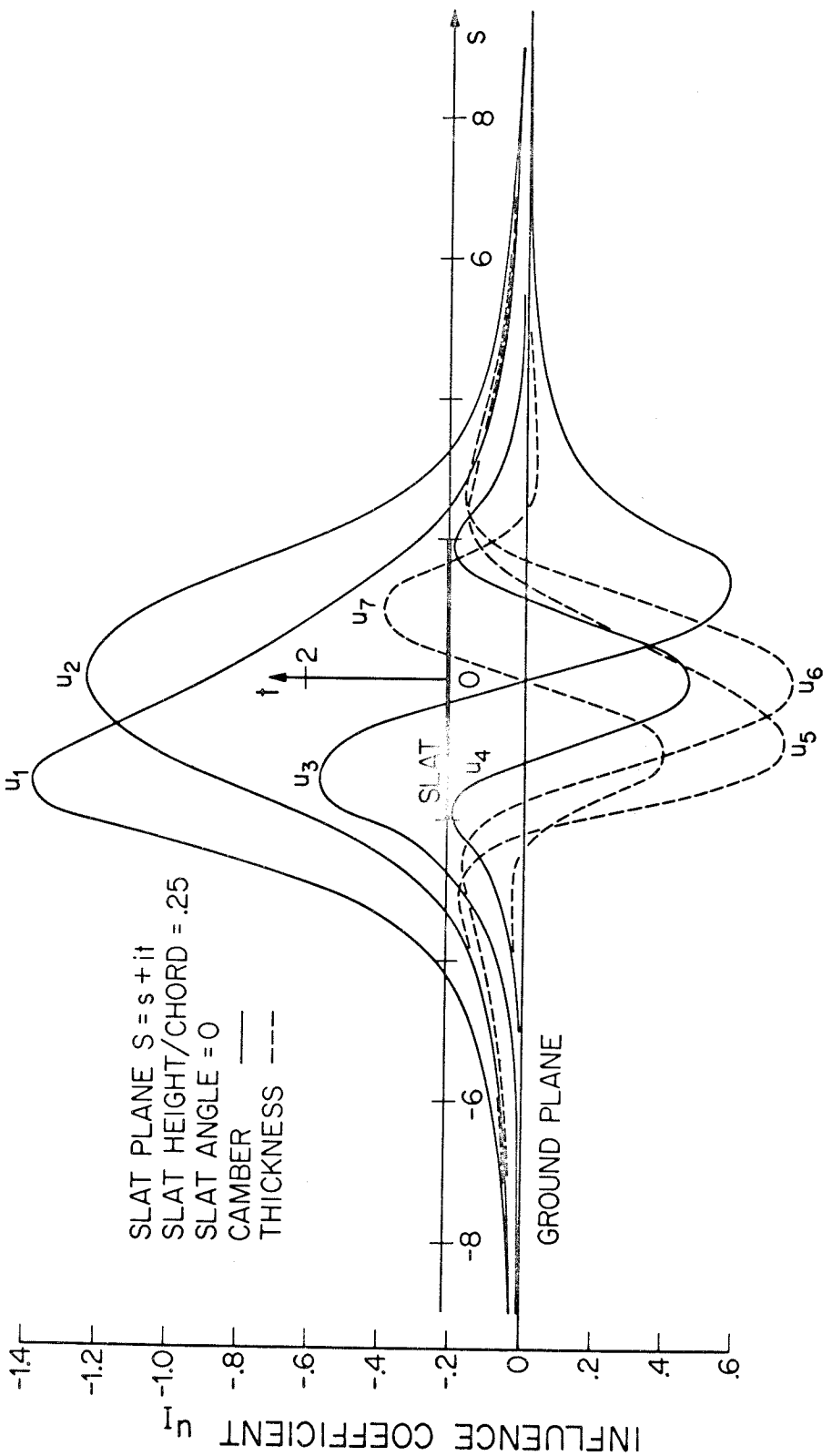

Figure 6C. Influence Coefficients

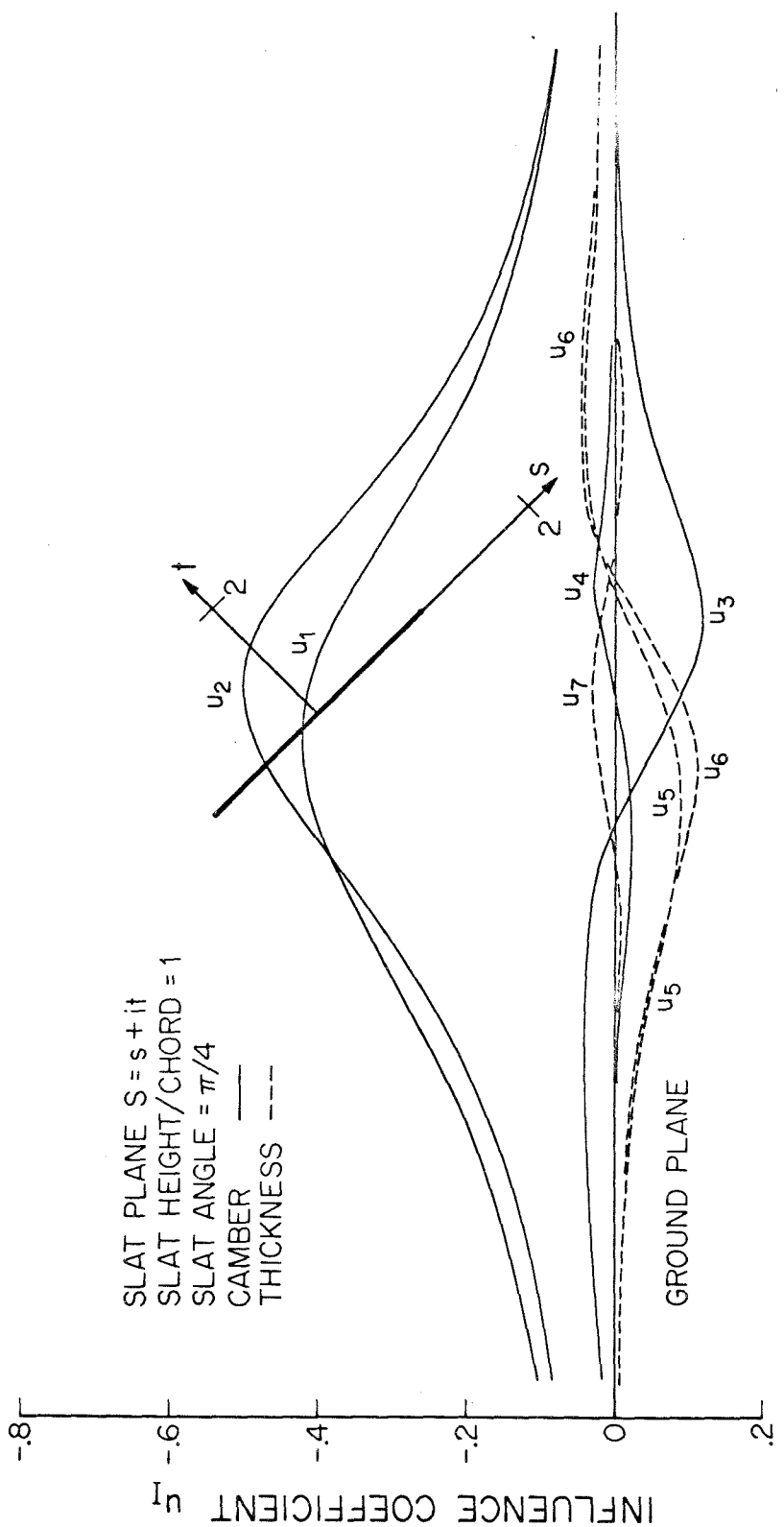

Figure 6D. Influence Coefficients

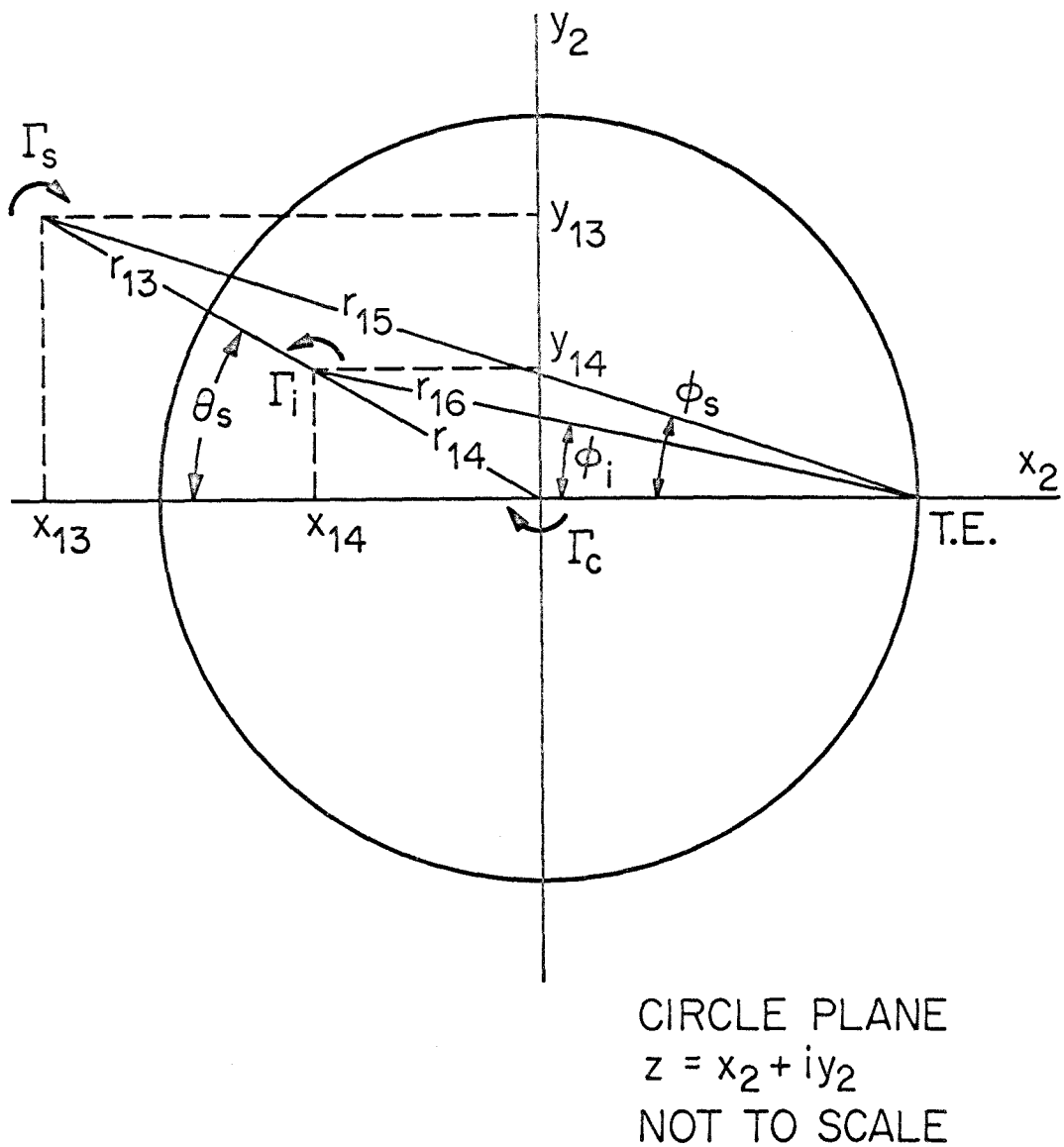

Figure 7. Slat and Image Slat Substitution Vortex Geometry

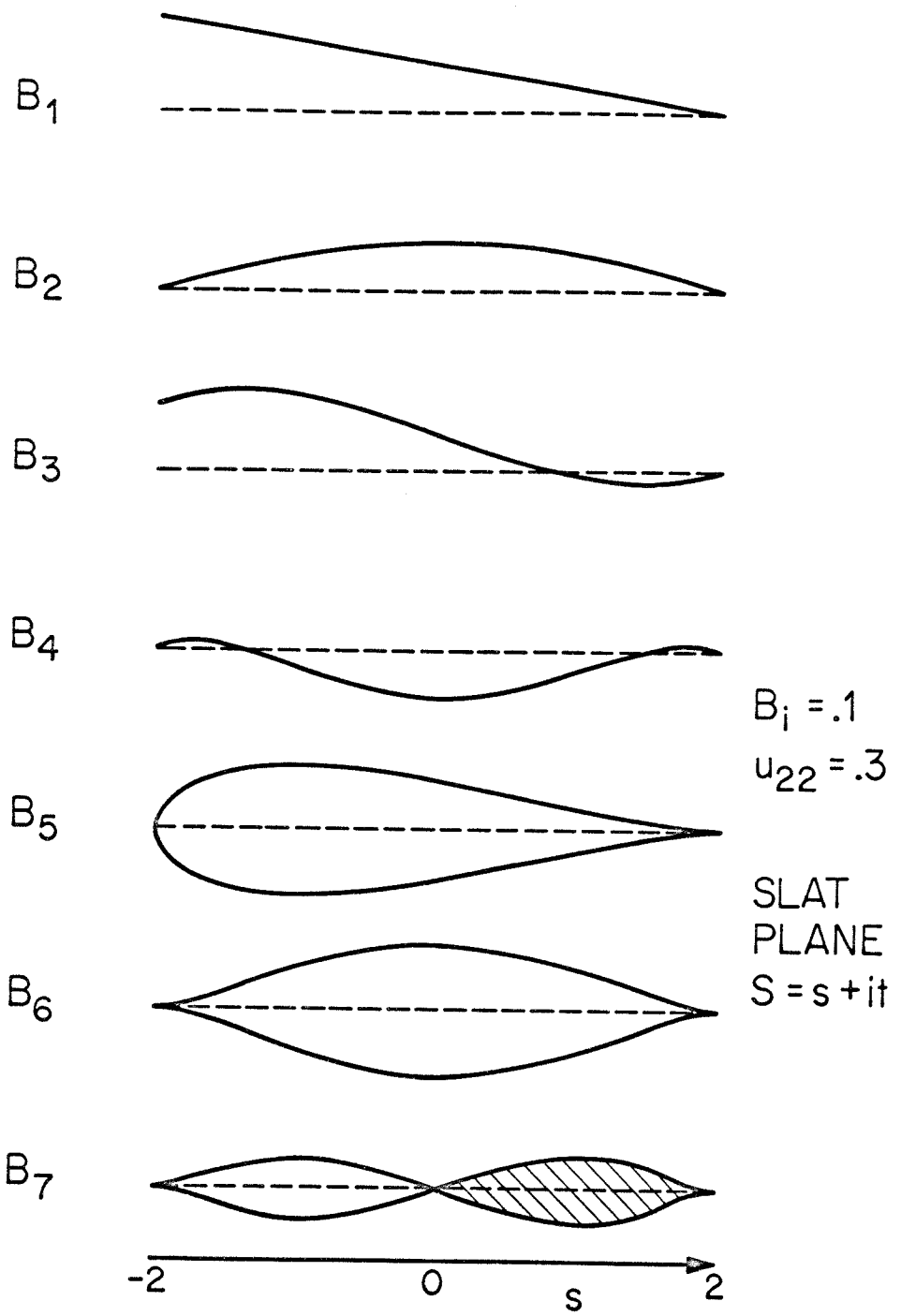

Figure 8. Slat Mode Shapes in Uniform Onset Flow

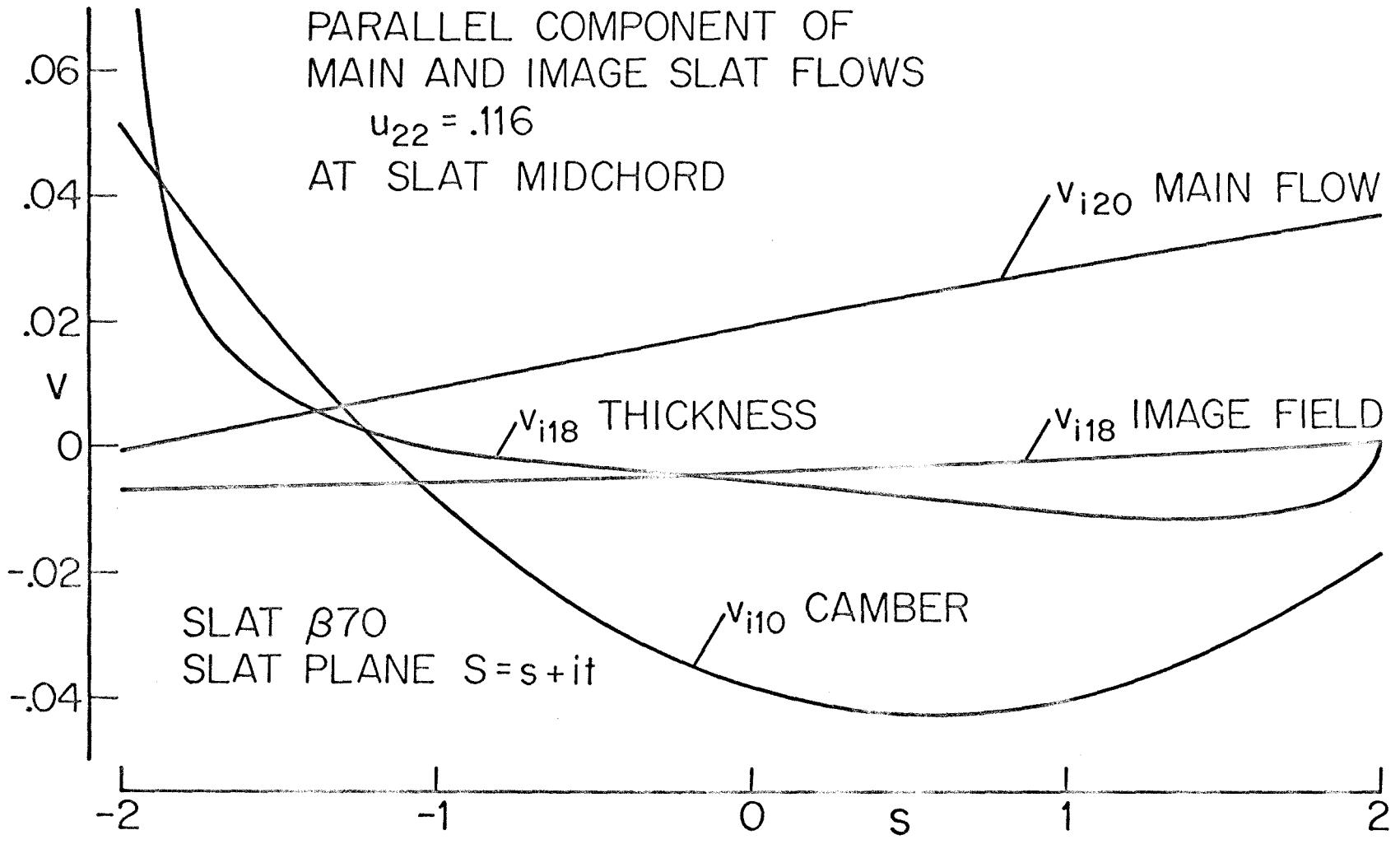

Figure 9. Normal Velocity Components on Slat Chord Line

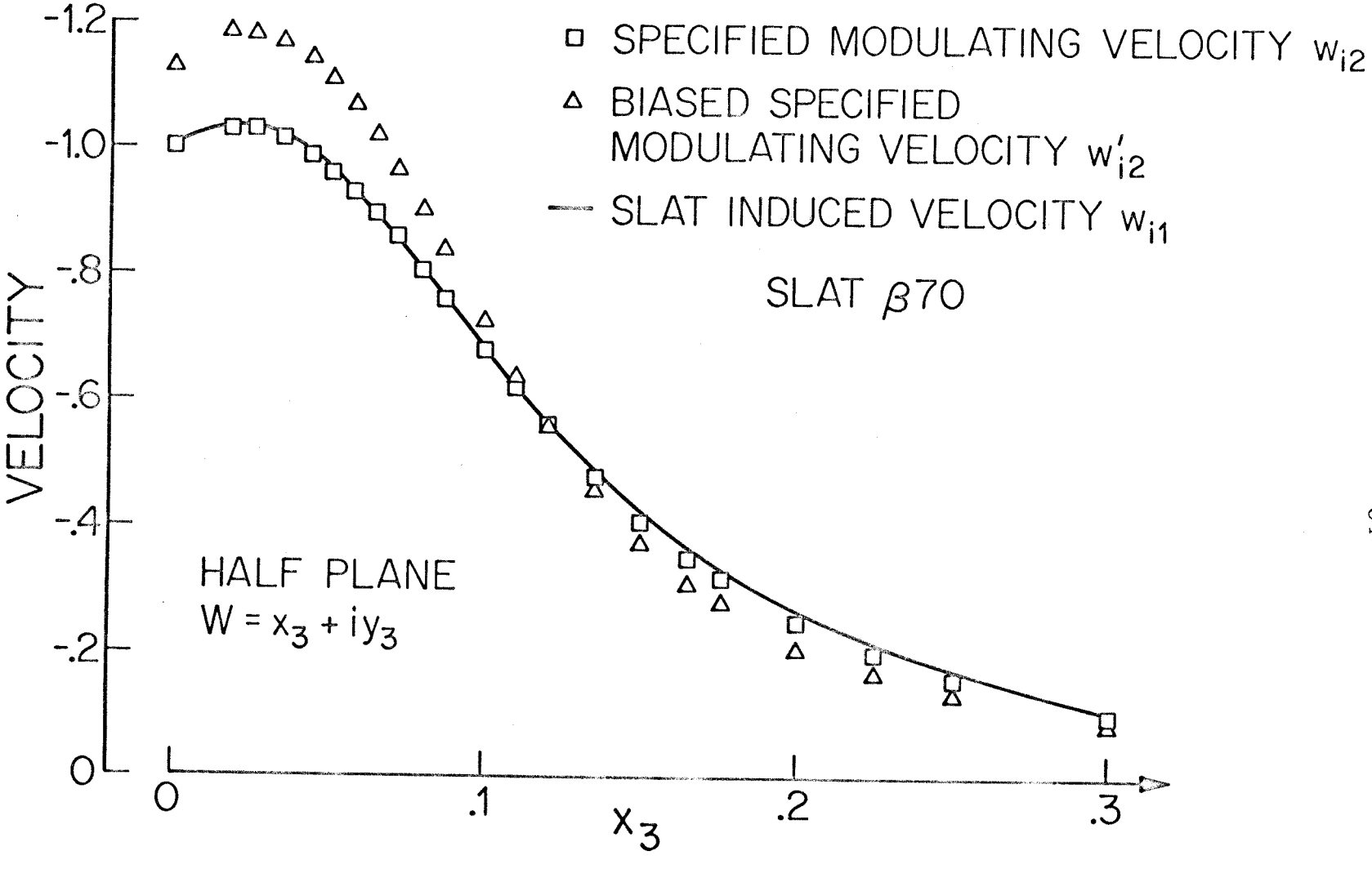

Figure 10. Modulating Velocity Distributions

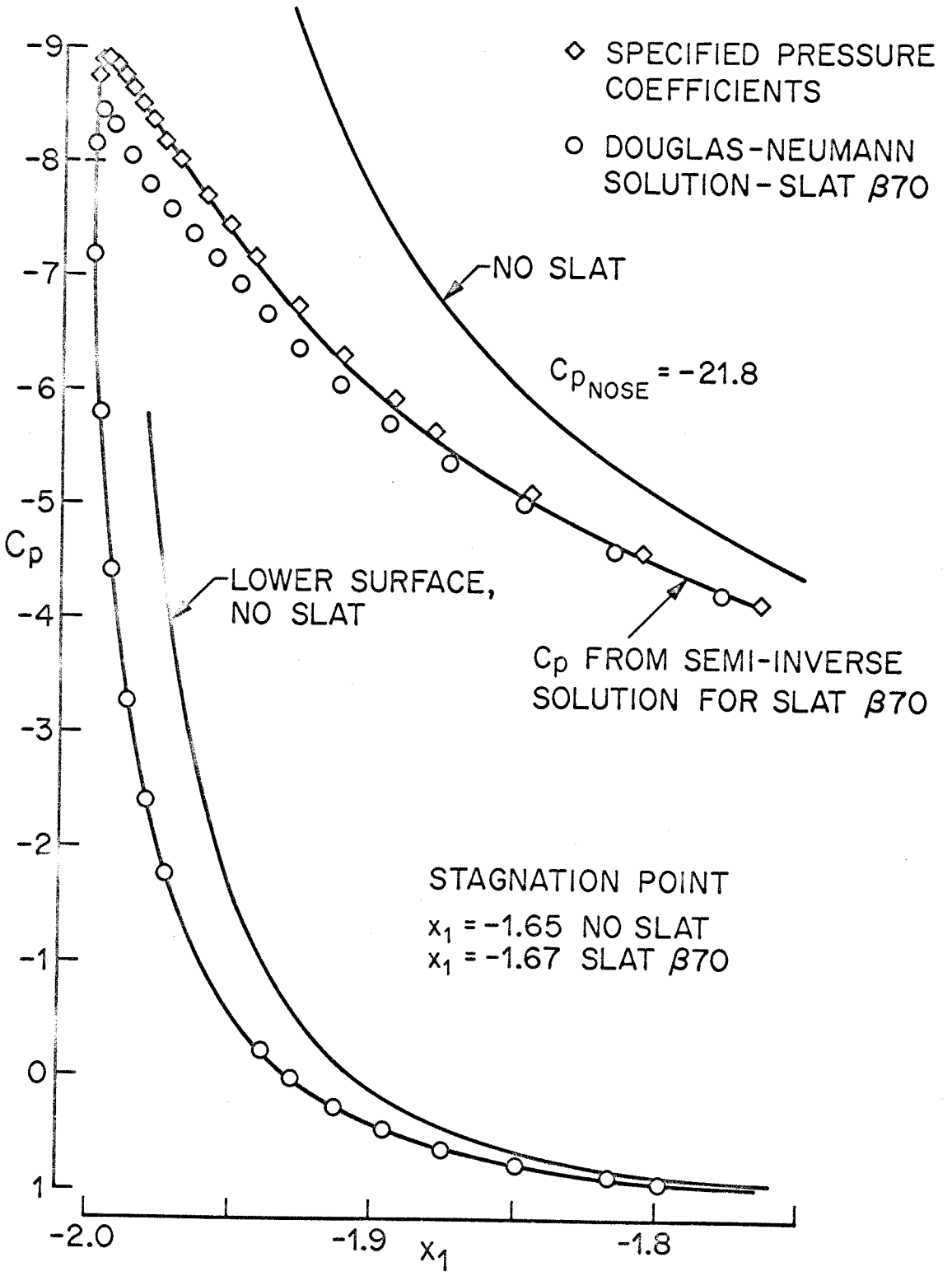

Figure 11. Pressure Distribution on Ellipse Nose

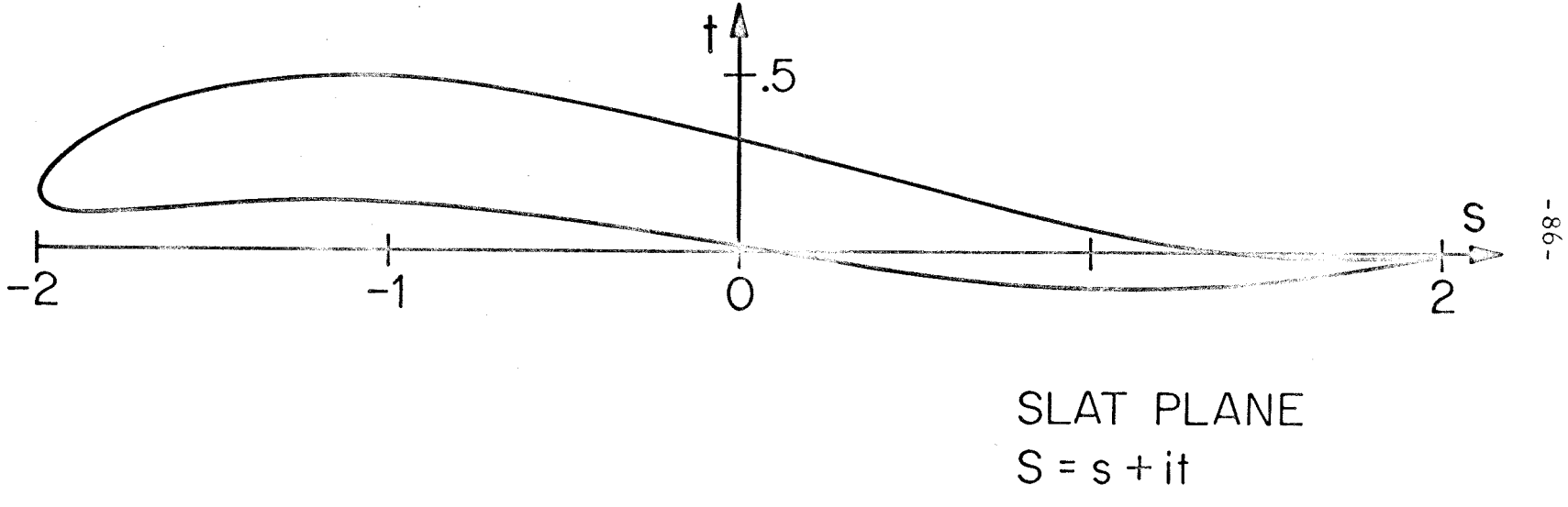

Figure 12. Slat β70 in Slat Plane

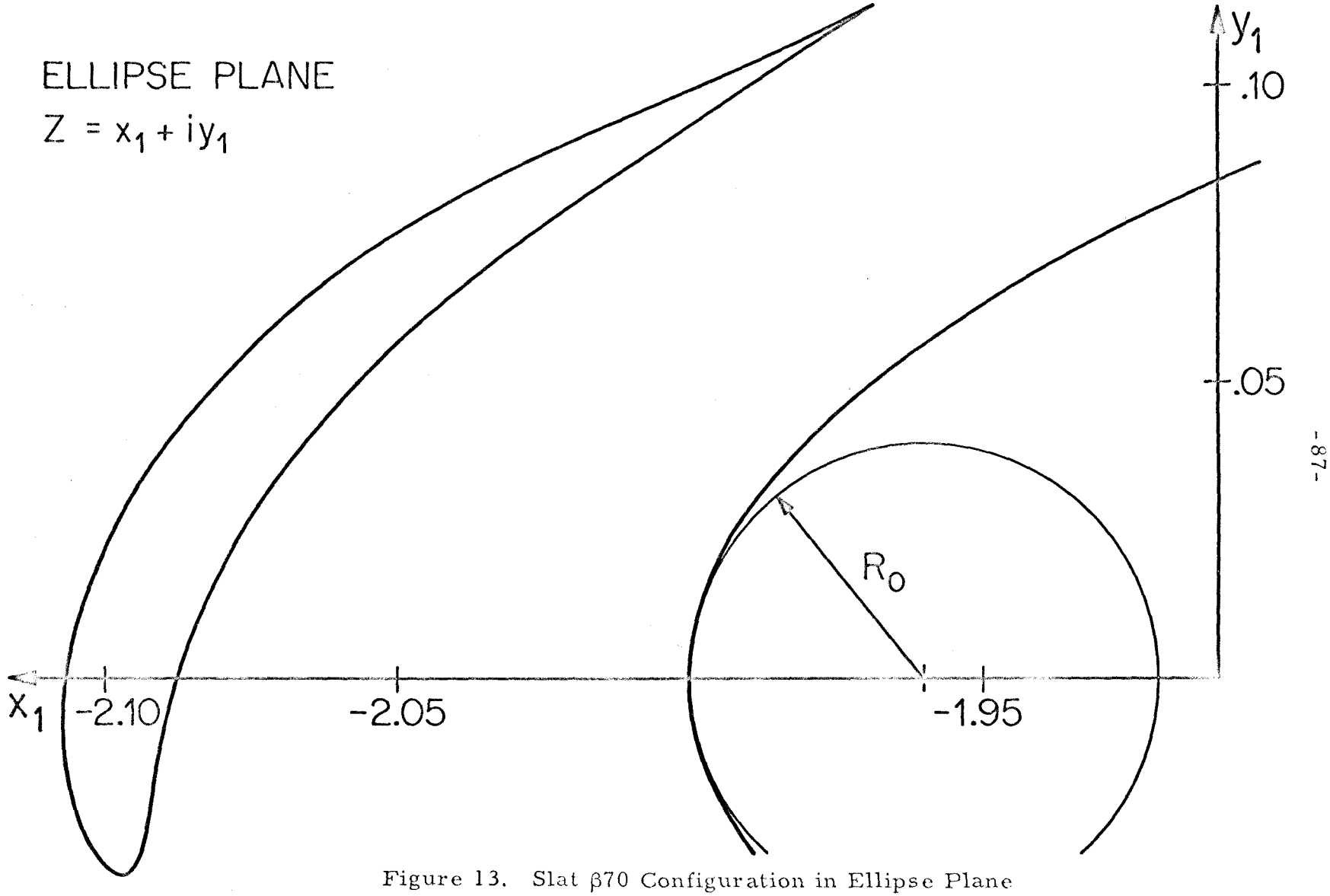

Figure 13. Slat β70 Configuration in Ellipse Plane

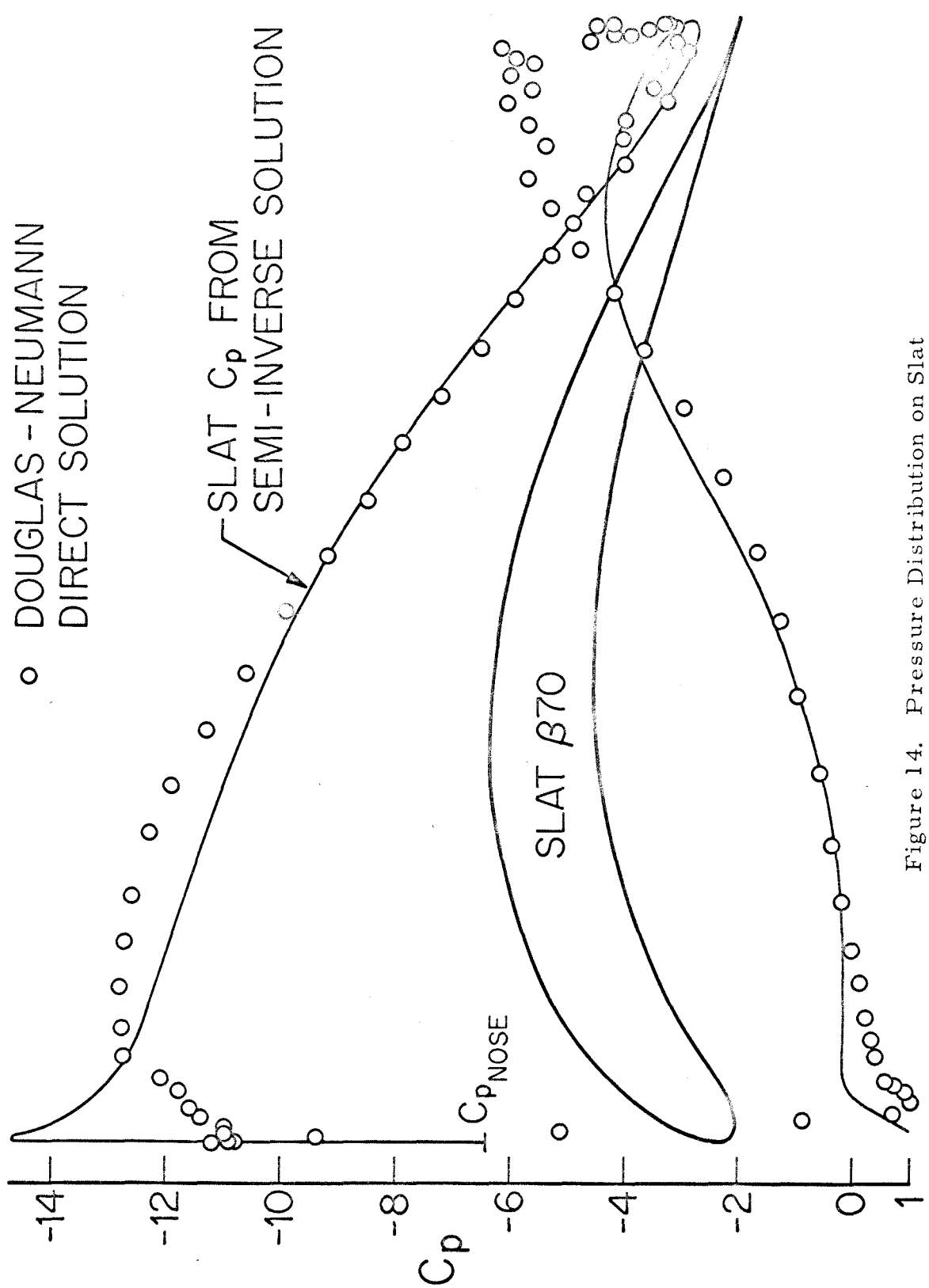

Figure 14. Pressure Distribution on Slat

APPENDIX

Parameter Values for Slat β70 Solution Slat Geometry

Chord $c_2 = .16$

Height $f_1 = .07$

Offset $f_2 = .05$

Angle $k_6 = .329$ (including first order correction)

Camber Mode Coefficients

$B_1 = 2.05 \times 10^{-2}$

$B_2 = 3.35 \times 10^{-2}$

$B_3 = 2.79 \times 10^{-2}$

$B_4 = 7.93 \times 10^{-4}$

Prescribed Thickness Mode Coefficients

$B_5 = 1.79 \times 10^{-2}$

$B_6 = 0$

$B_7 = -3.57 \times 10^{-3}$

Flow at Slat Midchord

Parallel component of main flow field $u_{20} = .127$

Parallel component of image slat field $u_8 = -.011$

Inclination .178

TABLE 1

Pressure Coefficients at the Matching Stations on the Ellipse - Slat β70

Matching Station Index	Ellipse Chord Station	Specified Pressure Coefficient	Solution Pressure Coefficient
i	x_{i1}	p_{i9}	p_{i12}
1	-2.0000	-7.9796	-7.9583
2	-1.9987	-8.7529	-8.7122
3	-1.9973	-8.8843	-8.8393
4	-1.9951	-8.9092	-8.8655
5	-1.9923	-8.8411	-8.8053
6	-1.9896	-8.7460	-8.7201
7	-1.9866	-8.6275	-8.6130
8	-1.9832	-8.4936	-8.4907
9	-1.9794	-8.3492	-8.3558
10	-1.9746	-8.1742	-8.1869
11	-1.9700	-8.0131	-8.0252
12	-1.9604	-7.6939	-7.6879
13	-1.9522	-7.4314	-7.3993
14	-1.9432	-7.1576	-7.0971
15	-1.9284	-6.7380	-6.6495
16	-1.9120	-6.3246	-6.2329
17	-1.8940	-5.9288	-5.8475
18	-1.8798	-5.6529	-5.5810
19	-1.8462	-5.0982	-5.0436

TABLE 1 (Cont'd)

Matching Station Index	Ellipse Chord Station	Specified Pressure Coefficient	Solution Pressure Coefficient
i	x_{i1}	p_{i9}	p_{i12}
20	-1.8073	-4.5919	-4.5496
21	-1.7647	-4.1560	-4.1218
22	-1.6697	-3.4633	-3.4391